Monthly Notices
of the
ROYAL ASTRONOMICAL SOCIETY

MNRAS **448,** 2900–2920 (2015) doi:10.1093/mnras/stv113

Coronal-Line Forest AGN: the best view of the inner edge of the AGN torus?

Marvin Rose,[1]★ Martin Elvis[1] and Clive N. Tadhunter[2]

[1]*Harvard–Smithsonian Center for Astrophysics, 60 Garden St, Cambridge, MA 02138, USA*
[2]*Department of Physics and Astronomy, University of Sheffield, Sheffield S3 7RH, UK*

Accepted 2015 January 16. Received 2015 January 16; in original form 2014 September 17

ABSTRACT

We introduce Coronal-Line Forest active galactic nuclei (CLiF AGN), AGN which have a rich spectrum of forbidden high-ionization lines (FHILs, e.g. [Fe VII], [Fe X] and [Ne V]), as well as relatively strong narrow (∼300 km s^{-1}) Hα emission when compared to the other Balmer transition lines. We find that the kinematics of the CLiF emitting region are similar to those of the forbidden low-ionization emission-line (FLIL) region. We compare emission line strengths of both FHILs and FLILs to CLOUDY photoionization results and find that the CLiF emitting region has higher densities ($10^{4.5} < n_{\rm H} < 10^{7.5}$ cm^{-3}) when compared to the FLIL emitting region ($10^{3.0} < n_{\rm H} < 10^{4.5}$ cm^{-3}). We use the photoionization results to calculate the CLiF regions radial distances ($0.04 < R_{\rm CLiF} < 32.5$ pc) and find that they are comparable to the dust grain sublimation distances ($0.10 < R_{\rm SUB} < 4.3$ pc). As a result, we suggest that the inner torus wall is the most likely location of the CLiF region, and the unusual strength of the FHILs is due to a specific viewing angle giving a maximal view of the far wall of the torus without the continuum being revealed.

Key words: galaxies: active – quasars: emission lines – quasars: general – galaxies: Seyfert.

1 INTRODUCTION

In the standard active galactic nuclei (AGN) unification model (Antonucci & Miller 1985) a large-scaleheight torus surrounds the inner AGN, obscuring our view of the central continuum source and the broad emission line region (BLR) from most directions. The inner wall of this torus lies at the sublimation radius of the most refractive dust – no dust can exist stably at smaller radii. This inner wall is heavily irradiated. It has been proposed that ablation of the surface produces a thermal wind of highly ionized gas (Krolik & Kriss 1995). This gas may produce an unusual spectrum, which may include forbidden high ionization lines (FHILs), also known as 'coronal lines' (Appenzeller & Wagner 1991).

From most orientations, either pole-on or edge-on, the torus inner wall will be barely visible. However, there should be a small range of angles of which the torus only just hides the inner nucleus. For these type 2 (dust obscured) AGNs, the rear inner wall will be maximally visible. Here, we describe a population of AGN that are candidates to be this special population – the Coronal Line Forest AGN (CLiF AGN).

In this paper, we introduce the CLiF AGN as a distinct class of AGN, and present data for a sample of the first seven identified CLiF AGN. The cosmological parameters used throughout this paper assume a Λ cold dark matter cosmology with parameters $\Omega_{\rm M} = 0.3$, $\Omega_\Lambda = 0.7$ and $H_\bigcirc = 70$ km s^{-1} Mpc^{-1}.

2 PROPERTIES OF CLIF AGN

Most AGN show some weak (EW < 3 Å) spectral lines from forbidden transitions of highly ionized ions (FHIL, ionization potential, $I_{\rm P} > 54.4$ eV; the He II edge) in their spectra, e.g. [Ne V], [Fe VII], [Fe X], [Fe XIV] (Penston et al. 1984).[1] The presence of FHILs in the spectra of AGN unambiguously indicate the presence of an AGN, due to their high ionization potentials, reaching up to soft X-ray energies ∼0.1–0.2 keV. FHILs are not generally associated with LINER nuclei or starbursts (Filippenko & Halpern 1984). FHILs are physically distinct because their transitions have higher critical densities ($n_{\rm C} \sim 10^{7.5}$ cm^{-3}; Osterbrock & Ferland 2006) than lower ionization species ($n_{\rm C} < 10^{6.0}$ cm^{-3}; Osterbrock & Ferland 2006). In most AGN, the FHILs are blueshifted (Δv ∼−250 km s^{-1}) with respect to the rest frame of the AGN and have substantial velocity widths (FWHM ∼ 1000 km s^{-1}), That are intermediate between those of the standard low-ionization forbidden lines (FLIL) of the narrow emission line region (NLR) (FWHM ∼500 km s^{-1}, e.g. [O III] λ5007), and the BLR (FWHM ∼ 5000 km s^{-1}). These kinematic properties support an origin for the FHIL emitting gas in

[1] In this work, we define $I_{\rm P}$ as the ionization potential required to achieve the current ionic stage by removing an electron from a lower ionization stage (De Robertis & Osterbrock 1984).

★ E-mail: mrose@cfa.harvard.edu

Table 1. Basic properties of the CLiF AGN sample. Redshifts ($z_{[O\,III]}$) are determined by single Gaussian fits to the prominent [O III] λ5007 emission line. The column r' gives the SDSS r' model magnitudes (https://www.sdss3.org/dr10/algorithms/magnitudes.php). We choose model magnitudes because these objects are type 2 AGN and therefore the photometry will be dominated by the host galaxy. In the cases of ESO 138 G1 and Tololo 0109-383, there are no available r' magnitudes, instead we use Cousins *R*-band magnitudes taken from Lauberts & Valentijn (1989). 'Spectrum' gives the origin of the spectrum. The column 'Ref' refers to the first publication that discusses the optical spectrum of the CLiF AGN candidate.

Name	RA (J2000)	Dec (J2000)	$z_{[O\,III]}$	r'	Spectrum	Ref.
Q1131+16	11:31:11.05	16:27:39.50	0.1732	17.31	WHT/ISIS	Rose et al. (2011)
III Zw 77	16:23:45.87	41:04:56.69	0.0341	15.25	SDSS	Osterbrock (1981)
Mrk 1388	14:50:37.85	22:44:03.61	0.0216	14.55	SDSS	Osterbrock (1985)
ESO 138 G1	16:51:20.13	−59:14:05.20	0.0091	13.02[a]	ESO	Alloin et al. (1992)
Tololo 0109-383	01:11:27.63	−38:05:00.48	0.0118	12.38[a]	IPCS/RGO	Fosbury & Sansom (1983)
J1241+44	12:41:34.25	44:26:39.25	0.0422	15.98	SDSS	This work
J1641+43	16:41:26.91	43:21:21.59	0.2214	18.60	SDSS	This work

[a]The *R*-band magnitude is from Lauberts & Valentijn (1989).

a wind outflowing from the BLR (Appenzeller & Wagner 1991) or the torus (Krolik & Kriss 1995).

A few rare AGN have instead a dozen or more FHILs with relatively high fluxes (F(FHIL)/F(Hβ) > 0.25): we call these the CLiF AGN. So far, CLiF AGN have only been identified serendipitously. Indeed, there are just five CLiF AGN in the literature (Table 1): Q1131+16 (Rose et al. 2011), III Zw 77 (Osterbrock 1981), Mrk 1388 (Osterbrock 1985), ESO 138 G1 (Alloin et al. 1992) and Tololo 0109-383 (Fosbury & Sansom 1983).

The optical spectra of these objects are remarkable in several ways. As well as the typical FLILs, i.e. [O III], [N II], [O I] and [S II], and the Balmer emission lines including Hα, Hβ, their spectra show many FHILs, including [Fe V], [Fe VI], [Fe VII], [Fe X], [Fe XI], [Ne V] and [Ar V] all with F(FHIL)/F(Hβ) > 0.2. This is more than found in typical AGN which just show the [Fe VII] λλ5721, 6087 lines (Appenzeller & Wagner 1991), and even these are weak (EW < 3 Å).

We find 10 unusual properties of CLiF AGN.

(1) Detection of the [Fe VII] lines 3759Å, 5159Å, 5720Å and 6087Å with the flux ratio F([Fe VII] λ6087)/F(Hβ) > 0.25. Where F(Hβ) is the flux from the *narrow* Hβ emission line.
(2) F([Fe X] λ6374)/F(Hβ) > 0.2.
(3) F([Ne V] λ3426)/F(Hβ) > 1.
(4) F([Fe V])/F(Hβ) & F([Fe VI])/F(Hβ) > 0.2.
(5) Hα/Hβ > 2.9 [the Case B value seen in the NLR; (Osterbrock & Ferland 2006)] *and* Hγ/Hβ ≈ 0.47 (Case B), implying that the apparent level of dust extinction calculated using Hα/Hβ is greater than that calculated using Hγ/Hβ.
(6) Higher level H I Balmer transitions (with wavelengths bluewards of Hδ and up to H_{16}; Rose et al. 2011) are present in emission.
(7) The FHILs are not blueshifted with respect to the FLILs ($\Delta v < 100\,km\,s^{-1}$).
(8) The velocity widths of the FHILs are narrow and the same as the FLILs (FWHM $\sim 300\,km\,s^{-1}$) using single Gaussian fits.
(9) The FHILs maintain their high equivalent widths (EWs) for longer than three years. This is long compared with the observed emission line fading times for Type IIn supernovae (Smith et al. 2009) and tidal disruption events for stars falling on to a supermassive black hole (SMBH; Gezari et al. 2006; Komossa et al. 2009; Wang et al. 2012), two astrophysical phenomena that also exhibit rich spectra of narrow emission lines including both FLILs and FHILs.
(10) High EW (>3 Å) emission lines from unknown/unexpected species are present.

This cluster of properties appear to be important for CLiF AGN. However, at this stage it is premature to formally define the CLiF AGN. We need a larger sample of CLiF AGN in order to produce a well-crafted definition.

3 A SEARCH FOR CLIF AGN IN SDSS

Given that CLiF AGN have very different spectral properties compared to typical AGN, one might expect that CLiF AGN would be easy to select. We used each of the unusual properties listed above that could be selected from the Sloan Digital Sky Survey (SDSS) DR10 data base.[2]

The properties of the emission lines in the SDSS spectra are determined using the BOSS pipeline (Bolton et al. 2012). Each line is modelled as a single Gaussian. The amplitudes, centroids, and widths of each emission line are optimized non-linearly to obtain a minimum-χ^2 fit to each emission line. All fitted emission lines are assumed to have the same redshift. The widths of the emission lines are assumed to have the same intrinsic velocity depending on the 'width group' they belong to. The relevant groups for the emission lines used in this work are 'Balmer' (consisting of the Balmer emission/absorption features) and 'emission' (consisting of non-Balmer emission lines). The velocity widths are a strength weighted average over the width group. The continuum level is estimated either from the best-fitting velocity-dispersion model if the spectrum is classified as a galaxy,[3] or from a linear fit either side of the emission line if the spectrum is classified as a quasar. The parameters such as the fluxes, FWHM, redshifts, EW and continua levels, as well as their associated uncertainties, are all reported by the BOSS pipeline (Bolton et al. 2012). We use EW instead of a flux ratio with Hβ because our definition for a strong FHIL as the ratio of the FHIL flux strength to the flux from the *narrow* Hβ emission line is not usable with the SDSS data base. As the SDSS data base does not differentiate between BLR and NLR Balmer emission, we cannot perform searches based on the flux ratios.

6 of the 10 CLiF properties could not be searched using the BOSS data base. Properties 1, 4 and 10 could not be selected because these Fe emission lines are not defined in the SDSS spectral fitting

[2] http://skyserver.sdss3.org/dr10/en/tools/search/sql.aspx
[3] The best-fitting velocity dispersion is determined by fitting locally for the position of the minimum-χ^2 versus trial velocity dispersion in the neighbourhood of the lowest gridded χ^2 value. See https://www.sdss3.org/dr10/algorithms/redshifts.php for a full description.

model (see table 5 in Bolton et al. 2012 for the full list of emission lines fitted by the SDSS). The kinematic properties 7 and 8 are not available in the BOSS data base either. Also, there is no timing information to determine whether property 9 is observed.

We attempted to select CLiF AGN candidates from the BOSS catalogue, making use of the online query tool, for properties 2, 3, 5 and 6.

(i) For property 2, Gelbord, Mullaney & Ward (2009) noted that the [Fe X] λ6375 broad blue wing is often blended with the [O I] λ6364 emission line which is included in the BOSS catalogue. As [O I]6300/6364 = 3 from atomic physics, if [Fe X] λ6375 is present and blended with [O I] λ6364, it will reduce the [O I]6300/6364 ratio. Hence we required that objects had to have [O I](6300/6364) < 3. A caveat is that [O I] λ6300 can also be blended with [S III] λ6312. This blend could result in a ratio [O I](6300/6364) > 3. However, the [S III] λ6312 emission line is included in the BOSS spectral fits (Bolton et al. 2012). This selection criterion will then be conservative because any contribution from [S III] λ6312 will result in CLiF AGN not being selected.

(ii) For property 3, we selected objects with strong [Ne V] λ3426 emission (EW[4] > 10 Å), although this only works for $z > 0.109$.

(iii) For property 5, we required that $H\alpha/H\beta > 2.9$ AND $H\gamma/H\beta < 0.5$, so as not to exclude reddened objects.

(iv) For property 6, we note that $H\epsilon$, which is in the BOSS spectral fits, has at $\lambda = 3970$ a wavelength close to that of [Ne III] λ3968 even closer than [O I] λ6364 and [Fe X] λ6375. Hence we created the criterion EW([Ne III] λ3968) > 5 Å[5] as $H\epsilon$ will boost the [Ne III] λ3968 flux.

Each of the initial searches based on only one of these properties resulted in large samples of several thousand objects. These were of unrelated phenomena, such as typical quasars whose broad emission lines altered both the Balmer decrements and [O I] ratios, resulting in false detections for properties 2 and 5. Property 3 also selected quasars which lacked strong Fe FHILs. Normal type 2 AGN were also selected with property 3, suggesting that this emission line is important in type 2 AGN (Mignoli et al. 2013). Finally property 6 selected both typical quasars and quiescent galaxies. These observations were confirmed with spot checks of their spectra.

Searches based on pairs of the criteria also failed to constrain the search. Therefore additional criteria were needed in order to constrain the search.

We then searched for objects using all four properties (2 AND 3 AND 5 AND 6). This search produced just two CLiF AGN. One of these was the previously detected Mrk 1388, and one new CLiF AGN: J1641+43.

As [Ne V] λ3425 limited the search to $z > 0.109$ we then scaled back the search to the three criteria excluding 3. This search found one additional CLiF AGN candidate: J1241+44.

These search criteria failed to find the known CLiF AGN III Zw 77, although it is in the SDSS data base. We obtained the SDSS spectrum for III Zw 77 separately.

While somewhat unsuccessful, this exercise serves to highlight both the apparent rarity of CLiF AGN in the AGN population, and the complexity of selecting such objects.

In this paper, we make use of SDSS spectra (Fig. 1). The basic properties of the CLiF AGN sample studied in this paper are given in Table 1. Note that the outputs of the SDSS pipeline are used only for the sample selection. Detailed measurements of emission line parameters such as the flux and velocity widths are measured using our own methods (Section 4). The redshifts were determined using single Gaussian fits to the [O III] λ5007 emission line. This line was chosen because it is the most prominent emission line in the optical spectra of these and most other AGN.

4 EMISSION SPECTRA

In Fig. 1, we plot the spectra for the four CLiF AGN with SDSS spectra. There is a remarkable number of emission lines. We performed a uniform line detection process by making fits to the lines and identifying them as described below.

4.1 Line detection

All line detections were determined by fitting single Gaussians to the emission features in the CLiF AGN spectra, using the Starlink package DIPSO,[6] accepting those with S/N > 3. We define S/N as the total flux measured using the Gaussian profile divided by the uncertainty of this flux from the fit as provided by DIPSO. For the three CLiF AGN without SDSS spectra (Q1131+16, ESO 138 G1 and Tololo 0109-373), we use the spectra and data presented in Table 1. 30–99 lines were found in the CLiF AGN (Table 2).

Single-Gaussian profiles, did not always provide adequate fits to the wings or peaks of the strongest lines (EW > 10 Å).[7] It is clear that these fits are inadequate for most of the CLiF AGN as the fitting residuals from the single Gaussian fits are large for the strong lines (Figs 3–5).

To address this problem, double-Gaussian models were fitted to the strong spectral lines. To produce the models, both broad and narrow Gaussians were fitted to the $H\beta$ and [O III] line profiles, where the narrow component widths for the $H\beta$ and [O III] lines are linked, yet the line centres, intensities and broad $H\beta$ width are free parameters. All but J1241+44 required a double-Gaussian model to fit these emission lines. Figs 2–5 show the residuals for the one and two-Gaussian fits to the [O III] λλ4959, 5007 emission lines. The variations shown in the residual plots of the fitting models used to obtain the emission line fluxes are dominated by noise in the continua of the spectra. Intrinsic velocity widths for the Gaussian components were obtained by correcting each of the components' FWHM in quadrature using the SDSS instrumental width of ∼3 Å. The intrinsic kinematics of the narrow (N) and broad (B) components are given in Table 3.

The parameters from the double-Gaussian fits were then used to fit all the strong (EW > 3 Å) emission lines throughout the CLiF AGN spectra (FWHM, velocity shift and relative amplitudes).

The fits for the weakest lines (EW ≤ 3 Å) were overestimated with the double-Gaussian model because the broader component required by the double-Gaussian model tended to fit the local continuum. In these cases a single-Gaussian fit was sufficient. We indicate

[4] While EW has been used as a standard indicator of emission line strength, it depends on the intensity of both the emission line and underlying continuum. Therefore, there is a caveat when defining the properties of CLiF AGN using the EW because the large observed EWs could be due to a weak stellar or AGN continuum emission.

[5] Tests of lower (∼3 Å) EW limits returned larger samples of several thousand unrelated objects, and higher (∼10 Å) EW limits produced no CLiF AGN at all.

[6] http://starlink.jach.hawaii.edu/starlink

[7] These include $H\alpha$, $H\beta$, [O II] λλ3726, 3729 [O III] λλλ4363, 4959, 5007, [N II] λ6583 and [Fe VII] λ6087.

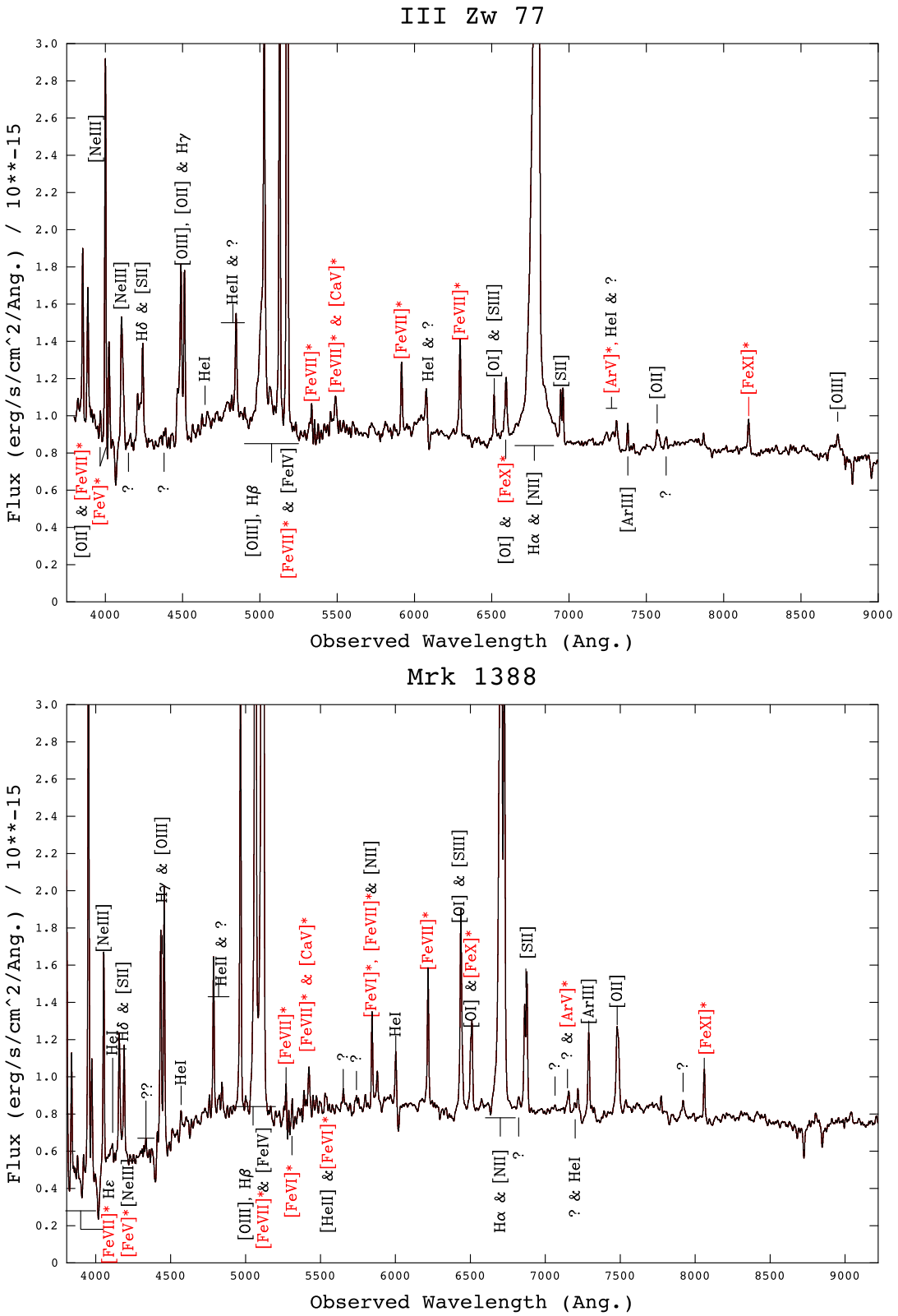

Figure 1. Labelled SDSS spectra for III Zw 77 and Mrk 1388. FHILs are labelled in red and marked with *. Note that we could not label all the emission lines on the spectra due to space constraints. The flux scale is measured in units of 10^{-15} erg s^{-1} Å^{-1} cm^{-2}, the observed wavelength is measured in units of Å. Labelled SDSS spectra for J1241+44 and 1641+43. The flux scale is measured in units of 10^{-16} erg s^{-1} Å^{-1} cm^{-2}.

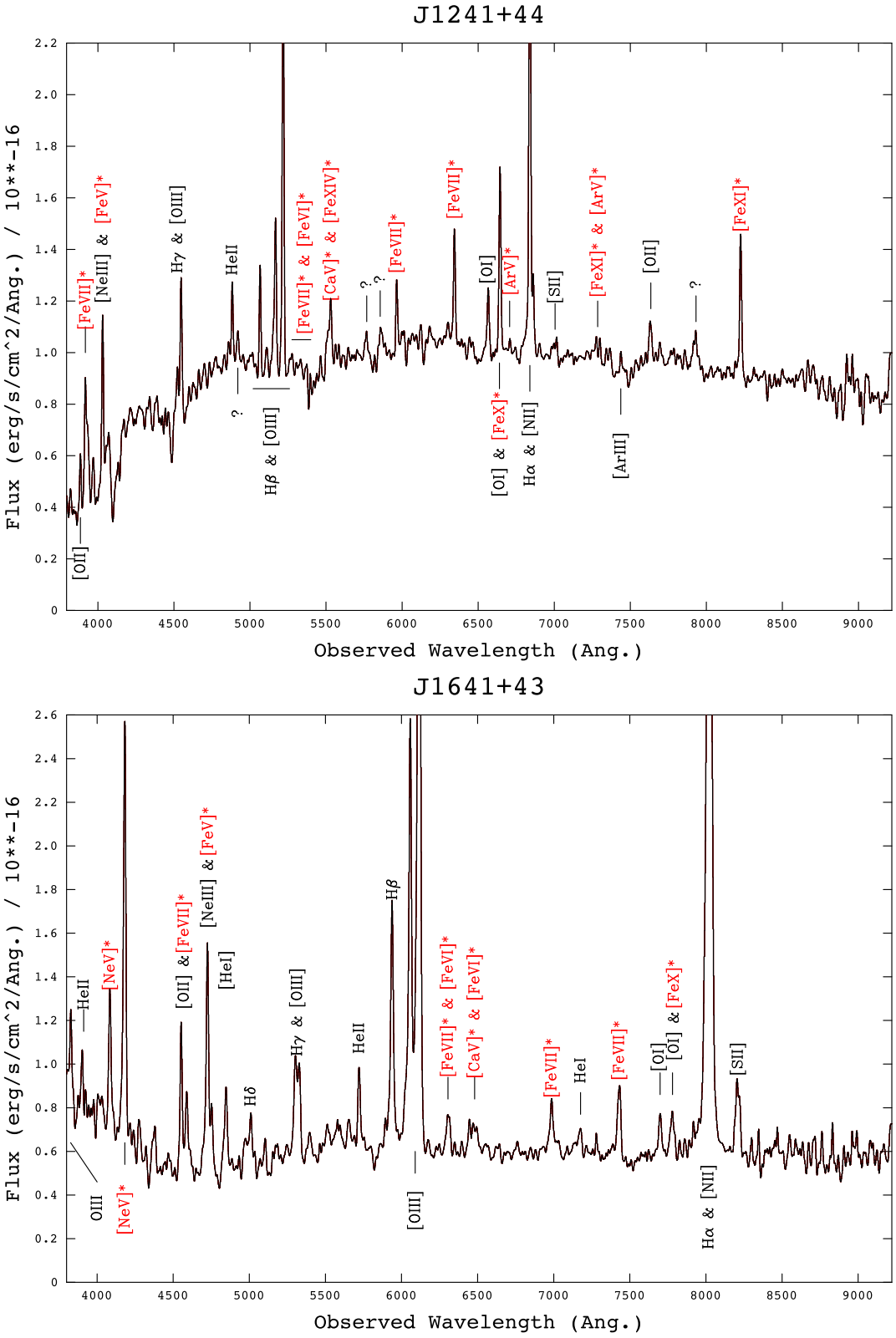

Figure 1 – *continued*

the number of Gaussians required to fit each individual emission line in Tables A1–A4.

We also take in to account constraints that are fixed by atomic physics. The [O III] λλ4959, 5007 doublet was modelled using the constraint that they have the same FWHM, a 1:3 intensity ratio and the line centre of λ4959 fixed relative to the centre of λ5007. The same approach was used for the [O I] λλ6300, 6364 (3:1 ratio) doublet blend (blended with [S III] λ6312 and [Fe X] λ6375) and the

Table 2. Key results from the optical spectra of the CLiF AGN. '$N_{\rm Lines}$' refers to the total number of emission lines with S/N > 3, $N_{\rm FHIL}$ is the number of detected FHILs, $N_{\rm [Fe\ VII]}$ is the number of [Fe VII] lines, $N_{\rm Fe}$ is the total number of iron emission lines, [Fe VII]/Hβ is the Hβ flux ratio for the [Fe VII] λ6087 emission line, [Fe X]/Hβ is the Hβ flux ratio for the [Fe X] λ6375 emission line, [Ne V]/Hβ is the Hβ flux ratio for the [Ne V] λ3425 emission line, $N_{\rm H\,I}$ is the number of detected H I lines and $N_?$ is the number of unidentified lines. The column 'BL' indicates whether broad emission lines were detected in the optical spectrum. 'Y' means yes, '?' indicates tentative evidence and 'N' indicates a non-detection. All results were obtained using the Starlink package DIPSO.

Name	$N_{\rm Lines}$	$N_{\rm FHIL}$ $I_P > 54.4$ eV	$N_{\rm [Fe\ VII]}$	$N_{\rm Fe}$	[Fe VII]/Hβ	[Fe X]/Hβ	[Ne V]/Hβ	$N_{\rm H\,I}$	$N_?$	BL
Q1131+16	99	19	7	23	0.50	0.23	1.01	10	30[a]	?
ESO 138 G1	71	24	7	26	0.24	0.08	1.22	9	2	N
Mrk 1388	62	13	5	11	0.34	0.19	*b*	7	17	?
III Zw 77	51	13	6	11	0.39	0.21	*b*	8	6	Y[c]
J1241+44	34	12	4	9	1.11	1.88	*b*	3	3	N
Tololo 0109-383	31	11	5	8	0.28	0.26	0.57	6	d	N
J1641+43	30	8	4	7	0.50	0.21	1.73	4	1	N

[a]A few 'unknown' lines have been identified since Rose et al. (2011).
[b][Ne V] λ3425 is shifted out of the observed frame of the spectra for these objects.
[c]The BLR emission of III Zw 77 is significantly blueshifted (-675 ± 25 km s^{-1}) with respect to the NLR emission.
[d]There were no 'unknown' lines indicated in Fosbury & Sansom (1983).

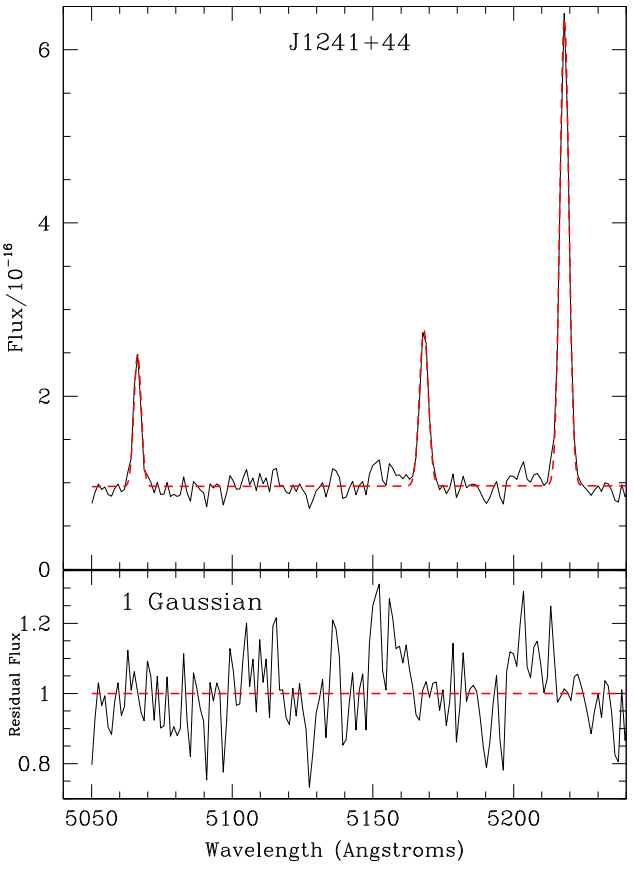

Figure 2. Top: multicomponent model fits to the Hβ and [O III] λλ4959, 5007 emission lines for 1241+44. The model fits are drawn with the dashed red line. The flux is measured in units of erg s^{-1} Å^{-1} cm^{-2} and the wavelength is in units of Å. Bottom: the residuals from the single Gaussian fits.

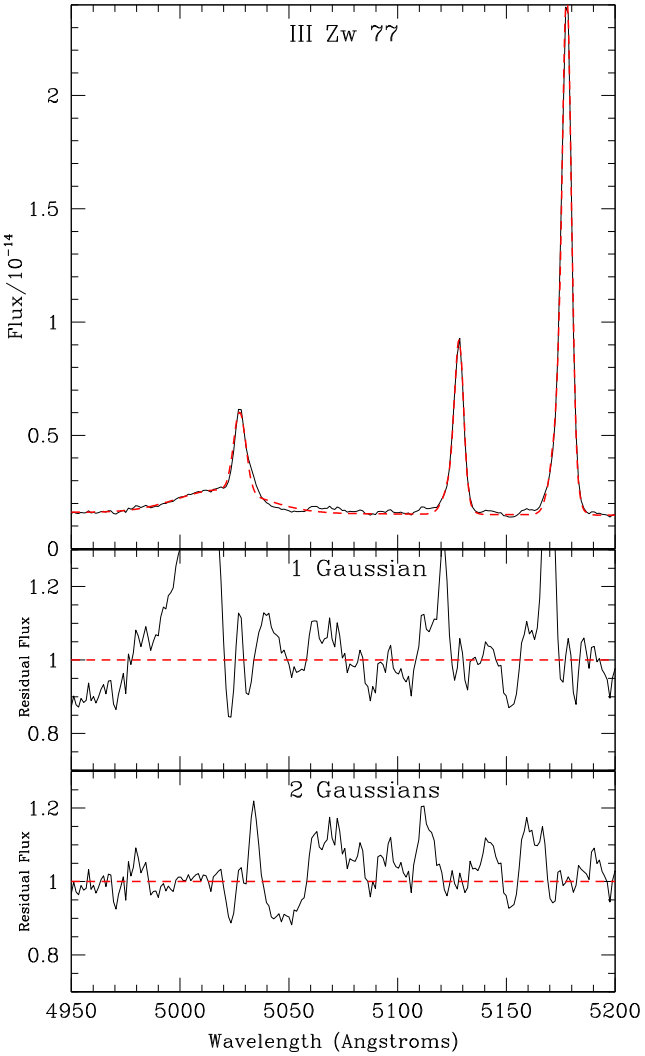

Figure 3. Top: multicomponent model fits to the Hβ and [O III] λλ4959, 5007 emission lines for III Zw 77. The model fits are drawn with the dashed red line. The flux is measured in units of erg s^{-1} Å^{-1} cm^{-2} and the wavelength is in units of Å. Middle: the residuals from the single Gaussian fits. Bottom: the residuals from the double Gaussian fits.

[N II] λλ6548, 6584 doublet (1:3 ratio), which is also often blended with the Hα emission line.

Throughout this paper, we use the summed fluxes of the two Gaussians. We do not use the data for weak emission lines (EW ≤ 3 Å) in any of the following investigation. The measured fluxes for the

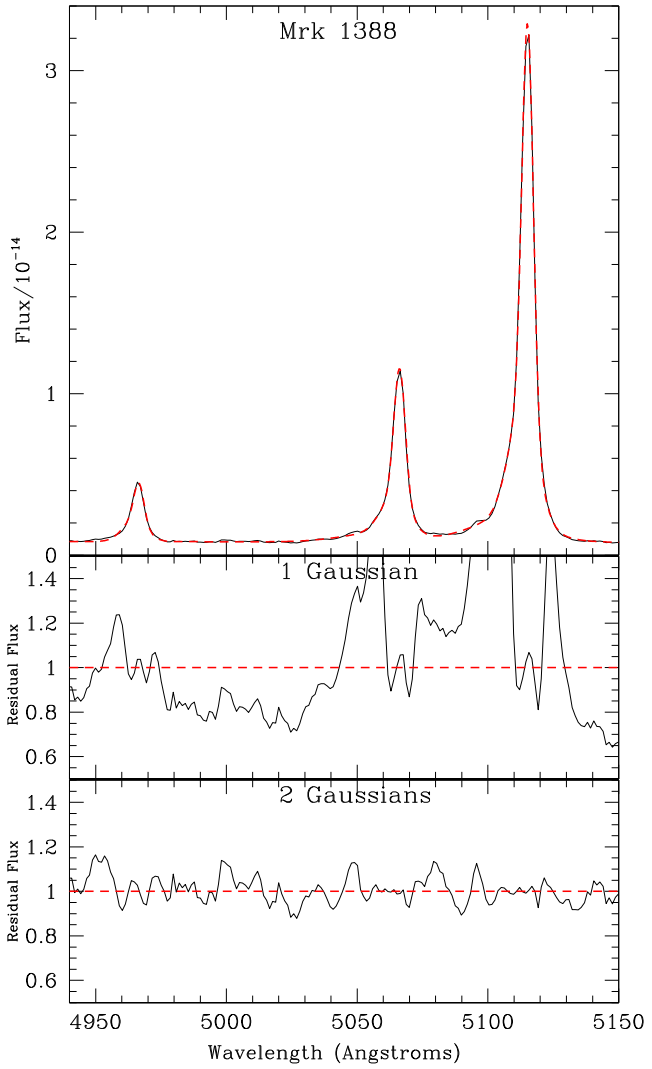

Figure 4. Top: multicomponent model fits to the Hβ and [O III] $\lambda\lambda$4959, 5007 emission lines for Mrk 1388. The model fits are drawn with the dashed red line. The flux is measured in units of erg s^{-1} Å^{-1} cm^{-2} and the wavelength is in units of Å. Middle: the residuals from the single Gaussian fits. Bottom: the residuals from the double Gaussian fits.

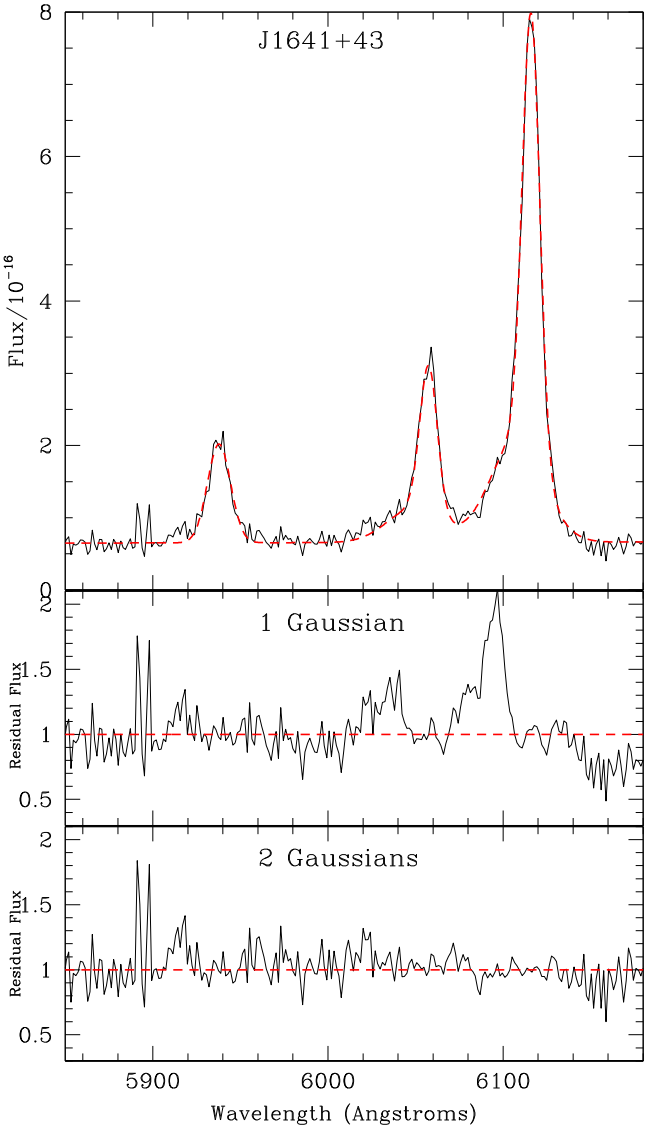

Figure 5. Top: multicomponent model fits to the Hβ and [O III] $\lambda\lambda$4959, 5007 emission lines for 1641+43. The model fits are drawn with the dashed red line. The flux is measured in units of erg s^{-1} Å^{-1} cm^{-2} and the wavelength is in units of Å. Middle: the residuals from the single Gaussian fits. Bottom: the residuals from the double Gaussian fits.

emission lines are presented for the SDSS CLiF AGN in Tables A1–A4 in the Appendix.

4.2 Line identification

We regarded an identification to be secure for an emission line if its line centre was within 1σ of the wavelength predicted for that particular emission line based on the redshift (as measured using the [O III] λ5007 emission line). We used Osterbrock (1981) to identify the majority of the emission lines in the CLiF AGN spectra. For the rest of the peculiar emission lines we used Meinel, Aveni & Stockton (1975) and Kaler (1976).

4.3 Emission line properties

The emission lines are of a wide variety including 9–26 FHILs and 1–30 unidentified lines (Table 2). A full list of the measured wavelengths, velocity widths (FWHM) and velocity shifts (Δv) for

Table 3. The double-Gaussian model parameters derived from the [O III] $\lambda\lambda$4959, 5007 and Hβ emission lines of the CLiF AGN spectra. The 'FWHM$_N$' and 'FWHM$_B$' columns present the rest-frame widths of the narrow and broad components of the model, which have been corrected for instrumental broadening. The 'Δv' column gives the rest-frame velocity separation of the broad relative to the narrow kinematic components. The 'Ratio' column give the amplitude ratio for the intensities of the broad to narrow components.

Name	FWHM$_N$ (km s^{-1})	FWHM$_B$ (km s^{-1})	Δv (km s^{-1})	Ratio.
III Zw 77	216 ± 11	512 ± 32	−127 ± 11	0.29
Mrk 1388	250 ± 21	723 ± 57	−106 ± 10	0.79
J1241+44	145 ± 9	–	−106 ± 10	–
J1641+43	563 ± 47	1770 ± 148	−412 ± 38	0.30

the emission lines are given in Tables A1–A4 in the Appendix. Below we discuss each group of emission lines.

4.3.1 Unidentified lines

CLiF AGN host unknown emission lines in their spectra. Such emission lines are not reported in typical AGN. Four CLiF AGN have 1–3, but III Zw 77, Mrk 1388 and Q1131+16 have 6, 17 and 30 unknown lines, respectively (Table 2). Only Q1131+16 and ESO 138 G1 share the same unknown emission lines. Q1131+16 has 2 and 3 in common unknown emission lines with J1241+44 and Mrk 1388, respectively. Mrk 1388 has 1 and 3 in common unknown emission lines with J1241+44 and III Zw 77, respectively. Finally, III Zw 77 and J1641+43 share 1 common unknown emission line.

4.3.2 FHILs

Each CLiF AGN has *at least* 10 FHILs. These FHILs are dominated by Fe ions, particularly [Fe VII] (Table 2; Tables A1–A4). All CLiF AGN show emission from [Fe VII] λλλλ3759, 5159, 5720, 6087, [Fe X] λ6375 and [Ca V] λ5307. The [Fe VII] λ6087 line is particularly prominent, with flux ratios [Fe VII]/Hβ of 0.24–1.11 (EW of 5–27 Å). However, in the spectra that cover [Ne V] λ3426, this line has flux ratios [Ne V]/Hβ of 0.57–1.73.

In addition, J1241+44 has [Ar V] λ6435 and [Fe XI] λ6985 that are not detected even in Q1131+16 and ESO 138 G1, the two CLiF AGN with the most FHILs.

4.3.3 Balmer emission lines

Strong (EW > 3 Å) higher level H I Balmer emission lines (Hϵ–H$_{16}$) are detected in 5/7 of the CLiF AGN (Table 2). Hydrogen emission from transitions with energy levels greater than Hϵ is not typically seen in AGN, implying some unusual physics in CLiF AGN, far from Case B. We investigate the H I emission of CLiF AGN in more detail in Section 5.1.

4.3.4 BLR emission lines

In this work, line width was not a selection criterion yet broad emission lines are not clearly detected in the spectra of the CLiF AGN suggesting a possible CLiF-type 2 AGN link. The exception is III Zw 77 in which the BLR Balmer emission lines are peculiarly blueshifted by -675 ± 25 km s^{-1} with respect to the NLR Balmer emission lines. This is an expected signature of a black hole recoil event, where after the merger of two SMBHs, anisotropic emission of gravitational waves gives a 'kick' to the resulting SMBH after the merger (e.g. see Favata, Hughes & Holz 2004; Civano et al. 2012). While this phenomenon is interesting in its own right, III Zw 77 is the only recoil candidate to date that is a CLiF AGN. This subject is beyond the scope of this work.

Rose et al. (2011) reported tentative evidence for broad emission at the base of the Hα+[N II] blend for Q1131+16. In this work, we assume that there is tentative evidence for a BLR if the Balmer recombination lines show broad wings that cannot be accounted for by using [O III] λ5007 as an NLR template. Only Mrk 1388 shows such evidence. The velocity width (FWHM) for this emission component is 1070 ± 160 km s^{-1}, however it is weak (represents 8 per cent of the flux of the blend) compared with the narrow Hα+[N II] blend and is not present for higher order Balmer emission.

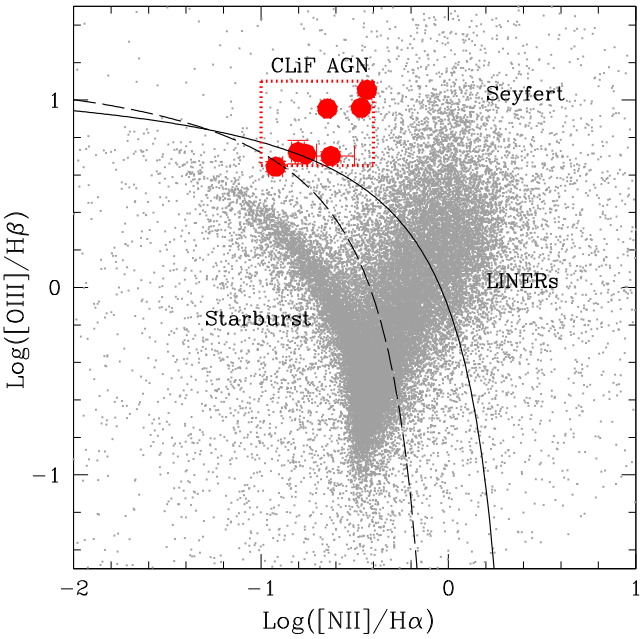

Figure 6. Diagnostic plot of Log$_{10}$([O III]/Hβ) versus Log$_{10}$([N II]/Hα). AGN are defined to lie above the solid line, H II-region like galaxies below the dashed line, and composite galaxies between these boundaries. The red circles represent the CLiF AGN. The small points represent objects detected by the SDSS and are taken from the SDSS-DR 7 release. The region outlined by the red dotted line is a 'CLiF AGN Region'.

5 RESULTS

5.1 A unique CLiF region on the BPT diagram

The Baldwin, Phillips & Terlevich (BPT) diagnostic diagrams use emission line ratios to determine whether the emission region of an object is photoionized by an AGN, or by a starburst (Baldwin, Phillips & Terlevich 1981; Veilleux & Osterbrock 1987; Kewley et al. 2006). In Fig. 6, we plot log$_{10}$([O III]/Hβ) versus log$_{10}$([N II]/Hα) for the CLiF AGN and SDSS emission line objects which include both AGN and starburst galaxies. The measurements for the SDSS objects were a subset (6000 objects) of the MPA-JHU SDSS DR7 release of spectrum measurements.[8] This subset is composed of measurements from objects with spectra which were reported to have the highest S/N, as well as having [O III]/Hβ and [N II]/Hα ratios which were consistent with the ranges shown in Fig. 6.

The SDSS AGN divide cleanly in the right-hand branch from star-forming galaxies in the left-hand branch. The solid line represents the extreme upper starburst line determined using the upper limit of theoretical pure stellar photoionization models (Kewley et al. 2001). The dashed line indicates the empirically derived boundary between H II region like galaxies and AGN (Kauffmann et al. 2003).

All the CLiF AGN fall in the cleft between AGN and the starburst galaxy branches. They are clearly removed from the main body of the SDSS AGN (grey dots) along the x-axis by log$_{10}$ [N II]/H$\alpha \sim 0.2$–1. Either the [N II] emission is weaker, or Hα is enhanced in CLiF AGN compared to typical AGN.

Balmer line recombination ratios are the most common tool to correct AGN spectra for intrinsic dust extinction assuming conditions close to Case B. The Hα/Hβ ratio is the favoured Balmer

[8] http://www.mpa-garching.mpg.de/SDSS/DR7/

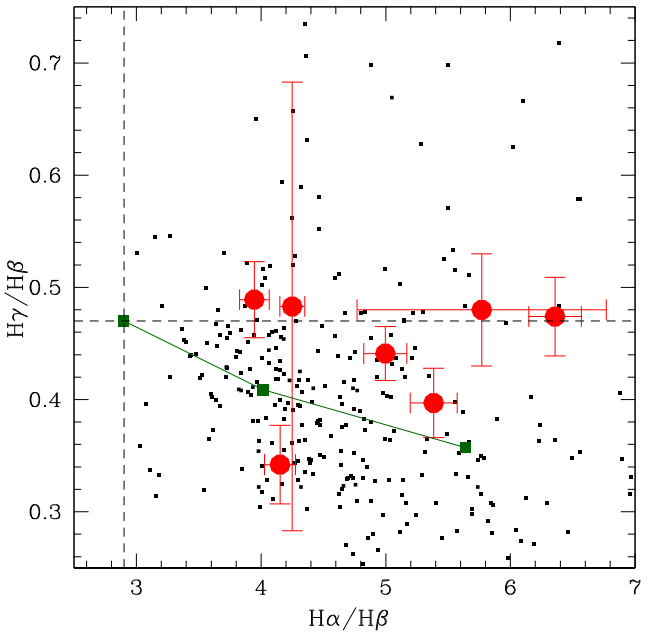

Figure 7. Plot showing Hγ/Hβ versus Hα/Hβ. The CLiF AGN are indicated by red circles and the type 2 AGN of Reyes et al. (2008) are indicated by black crosses. The theoretical Case B values for the decrements are indicated by the dashed lines. The dark green squares indicate the Balmer decrement values for reddening of $A_V = 1$ and 2 (labelled).

decrement for this task because these emission lines are the strongest and have the widest wavelength separation. However, the large number of Balmer lines from high-energy transitions shows that Case B does not apply to CLiF AGN (Rose et al. 2011).

In Fig. 7, we plot Hγ/Hβ versus Hα/Hβ for the CLiF AGN (red circles) and the type 2 AGN of Reyes et al. (2008, black crosses). We limit the Reyes et al. (2008) sample to $z < 0.42$ so that Hα lies in the SDSS spectrum, and use Balmer lines which have EW > 3 Å, leaving 325 out of the original 887 type 2 AGN. We use the SDSS pipeline measurements for the Balmer decrements of the type 2 AGN of Reyes et al. (2008).

A reddening line for Calzetti, Kinney & Storchi-Bergmann (1994) dust is shown with $A_V = 0$, 1 and 2 marked. Most of the type 2 AGN of Reyes et al. (2008) roughly follow the reddening trend indicated by the reddening line. Within the 1σ uncertainties 83 per cent have values consistent with the reddening line.

It is clear that while the Hα/Hβ ratios for the CLiF AGN all exceed the Case B values of 2.9 by up to a factor of ∼2, the majority of the Hγ/Hβ agree with the Case B value of 0.47 within the uncertainties (Table 4). These Case B values apply to the low density ($n_e = 10^2$–10^4 cm^{-3}) limit, with a temperature of 10 000 K (Osterbrock & Ferland 2006).

Table 4. The Hα/Hβ and Hγ/Hβ Balmer decrements for the CLiF AGN.

Name	Hα/Hβ	Hγ/Hβ
Q1131+16	5.00 ± 0.17	0.44 ± 0.02
ESO 138 G1	4.25 ± 0.10	0.48 ± 0.20
Mrk 1388	3.95 ± 0.12	0.49 ± 0.03
III Zw 77	4.15 ± 0.13	0.34 ± 0.04
J1241+44	6.36 ± 0.21	0.47 ± 0.04
Tololo 0109-383	5.77 ± 1.00	0.48 ± 0.05
J1641+43	5.38 ± 0.19	0.40 ± 0.03
Case B	2.9	0.47

Instead, 5/7 of the CLiF AGN are inconsistent with the reddening line. These objects all have Hα/Hβ ratios exceeding Case B, yet their Hγ/Hβ ratios are consistent with the Case B value. Only III Zw 77 and J1641+44 lie close to the reddening line and of these only III Zw 77 $> 2\sigma$ from case B Hγ/Hβ. It is likely that reddening does not dominate the CLiF AGN Balmer decrements.

A visual inspection of the spectra of the remaining 17 per cent of the type 2 AGN of Reyes et al. (2008) that do not follow the reddening line show that they are not CLiF AGN. Their positions on Fig. 6 are possibly due to uncertainties with the SDSS pipeline fits e.g. degeneracies with the Hγ+[O III] λ4363 blend.

5.2 Kinematics

We investigated the kinematics of the CLiF AGN with SDSS spectroscopy using the velocity shifts (Δv, and FWHM from the single Gaussian fits to the emission lines of the CLiF AGN because there are not enough lines for a broad and narrow component separation (Section 4.1).

5.2.1 *FWHM versus I_P*

In Fig. 8, we plot the velocity width (km s^{-1}) versus I_P (eV) for the emission lines detected in each of the CLiF AGN. There is significant scatter in the measured widths of a few hundred km s^{-1}. However, there is no trend for FWHM to increase with I_P.

There are four lines (blue crosses) which have much higher FWHM than the median of all the emission lines of the CLiF AGN (horizontal dashed lines). These emission lines are:

(i) [Ar V] λ7004 ($I_P = 59.81$ eV) in III Zw 77 which may be intrinsically broader, but could always be blended with an unknown emission line.

(ii) [Ca V] λ5309 ($I_P = 67.30$ eV) in III Zw 77 and J1241+44 possibly blended with [Fe XIV] λ5303.

(iii) Hγ blended with [O II] λ4415 in J1641+43. The low S/N of the blending companions leads to Gaussian fitting degeneracies which are not resolved.

The three CLiF AGN without SDSS spectra also show no trend for FWHM with I_P (Fosbury & Sansom 1983; Alloin et al. 1992; Rose et al. 2011). However, Alloin et al. (1992) found a median velocity width for all the emission lines (FLILs and FHILs) around 1000 km s^{-1} for ESO 138 G1, 2–3 times higher than found for the SDSS CLiF AGN sample.

5.2.2 *Δv versus I_P*

In Fig. 9, we plot the velocity shifts (Δv; km s^{-1}) relative to the [O III] λ5007 line, versus I_P (eV). Again there is significant scatter of a few hundred km s^{-1}. There is no evidence for a trend with I_P.

There are seven lines which have much larger Δv (blue crosses) than the median of all of the emission lines of the CLiF AGN (horizontal dashed lines). These emission lines are:

(i) [O II] λλ3726, 3729 doublet ($I_P = 13.61$ eV) in III Zw 77, Mrk 1388 and J1241+44, whose blended line centre (assumed to be 3727.4 Å) is dictated by the electron density of the emission region.

(ii) [O I] λ6364 ($I_P = 0$ eV) in Mrk 1388 which is in a blend with [Fe X] λ6375.

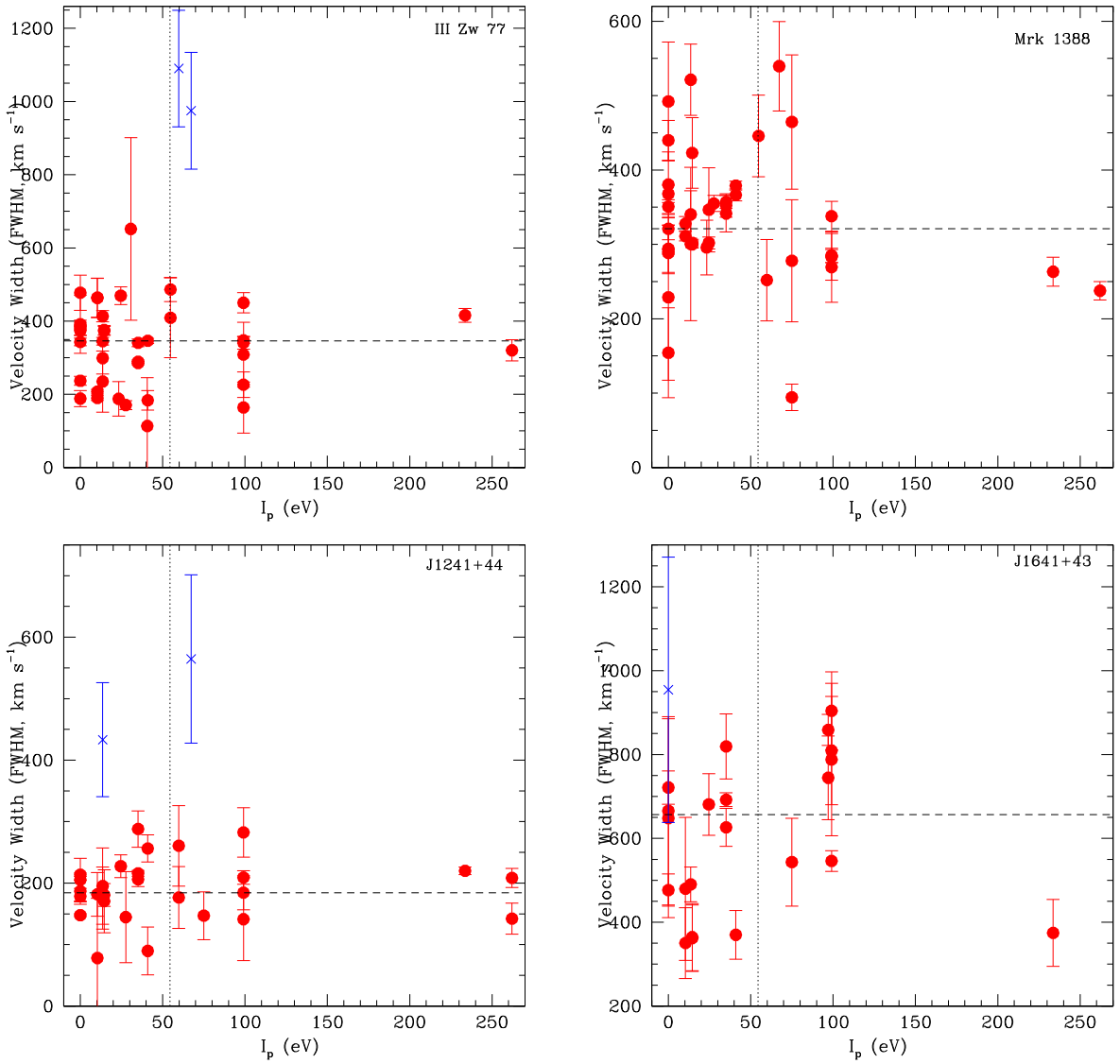

Figure 8. Velocity widths FWHM (km s^{-1}) for the single Gaussian fits to the emission lines versus I_P (eV) for the CLiF AGN (red circles). The blue crosses are for the emission lines which have a much higher FWHM than the median of all the emission lines of the CLiF AGN. The median velocity widths are indicated by the dashed lines. The dotted line indicates the boundary between the FLILs and FHILs ($I_P = 54.4$ eV; the He II edge).

(iii) [Fe XI] λ6984 ($I_P = 262.1$ eV) in J1241+44 an uncommon [Fe XI] emission line.

(iv) [Fe VII] λ5159 ($I_P = 99.1$ eV) in J1241+44 and [Fe VI] λ5176 ($I_P = 75.0$ eV) in J1641+43 both of which are blended with each other.

The outliers in blends are likely the result of fitting degeneracies. For the [Fe XI] λ6984 line, it is possible that this emission line has been misidentified.

Q1131+16 also shows no trend for Δv with I_P (Rose et al. 2011). Unfortunately, Fosbury & Sansom (1983) and Alloin et al. (1992) do not comment on Δv for the FHILs.

5.3 The [O III] λ4363 emitting region

The emission-line flux ratio of the FLILs [O III] 4363/5007 is a widely used diagnostic for the ionization mechanism and temperature of NLR in AGN (Osterbrock & Ferland 2006) as it has little or no contamination from star formation compared to other NLR (e.g. [N II], [S II] and [O I]). However, [O III] λ4363 has a 50 times higher critical density ($n_C = 10^{7.6}$ cm^{-3}; Osterbrock & Ferland 2006) than [O III] λ5007 ($n_C = 10^{5.8}$ cm^{-3}), comparable to those of the FHILs.

Nagao, Murayama & Taniguchi (2001) showed that, like [Fe VII], the [O III] 4363/5007 ratio increases across Seyfert galaxy types from type 2 to type 1. This suggests that a significant portion of the [O III] λ4363 flux may be emitted from the [Fe VII] emitting clouds in the CLiF region.

We address this possibility directly in Fig. 10 where we plot the strength of [O III] λ4363 against [Fe VII] λ6087. Both values are normalized to [O III] λ5007 to eliminate AGN luminosity as a variable. Fig. 10 includes both the CLiF AGN and the Erkens et al. (1997) FHIL sample. Erkens et al. (1997) observed a sample of 15 Seyfert galaxies and two emission line radio galaxies based on the presence of FHILs in previous work. For both CLiF AGN, and the narrow-line Erkens et al. (1997) samples, there is a clear correlation of [O III] λ4363 with [Fe VII] λ6087. The correlation

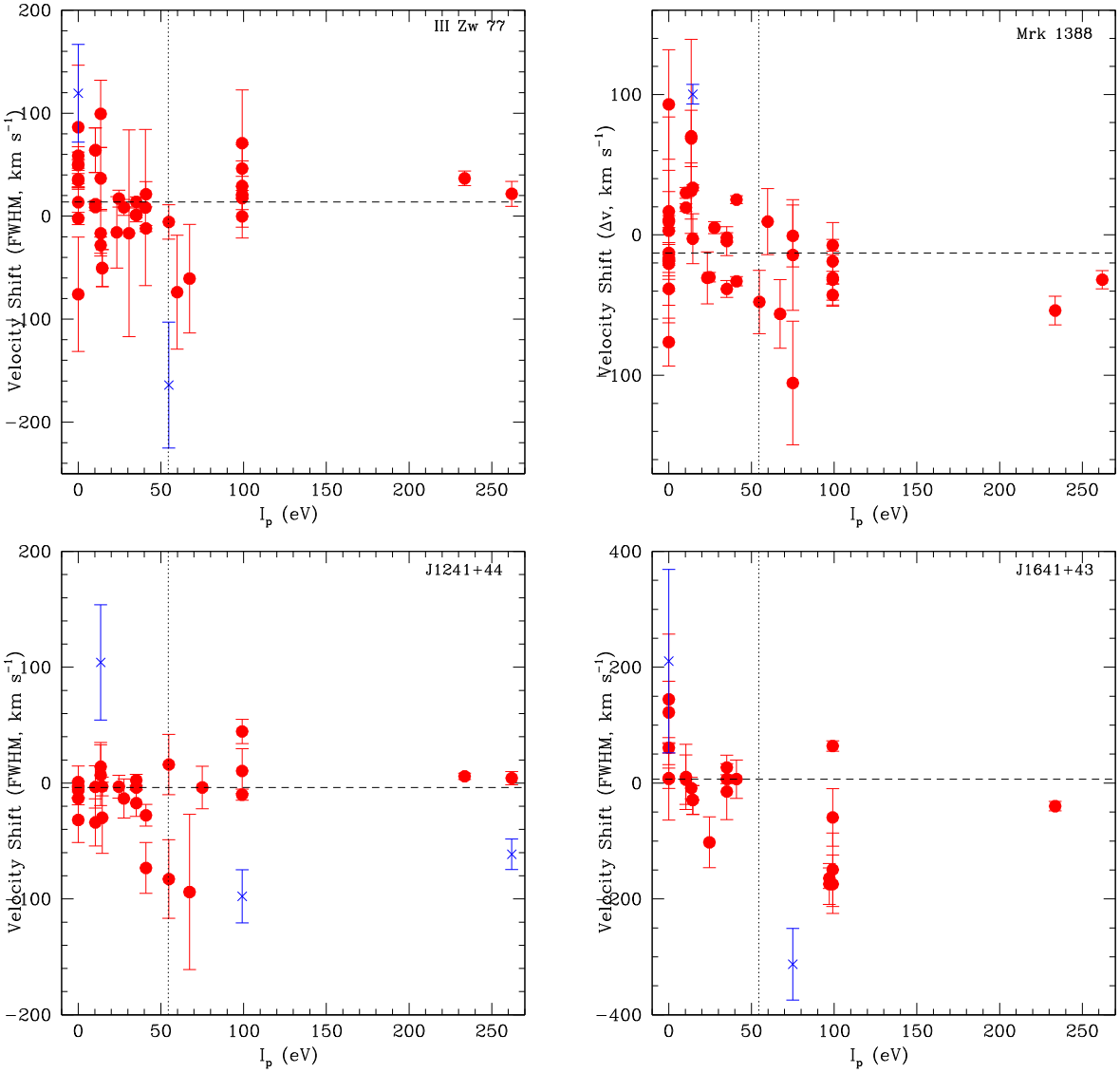

Figure 9. Velocity shift (km s^{-1}) with respect to the redshift of the CLiF AGN for the single Gaussian fits to the emission lines versus I_P (eV) for the CLiF AGN (red circles). The blue crosses are for the emission lines which have a much much larger Δv than the median of all of the emission lines of the CLiF AGN. The median velocity shifts are indicated by the dashed lines. The dotted line indicates the boundary between the FLILs and FHILs ($I_P = 54.4$ eV; the He II edge).

coefficient for these objects is $R = 0.92$. Using Spearman's rank correlation test, this correlation is statistically significant, with a p-value = 0.05 per cent.

This correlation clearly indicates that both the [Fe VII] and [O III] λ4363 fluxes are emitted from the same emission region in both CLiF AGN and in the narrow-line Erkens et al. (1997) AGN i.e. the CLiF region. Given that the FHILs in both the CLiF AGN and Erkens et al. (1997) narrow-line AGN samples share the same kinematics as the FLILs, this correlation suggests a strong link between the FHIL emitting clouds and the [O III] λ4363 emitting clouds.

The broad-line Erkens et al. (1997) AGN show no such correlation ($R = -0.01$, $p = 0.98$). In the broad-line Erkens et al. (1997) objects FHILs do not share the same kinematics as the FLILs, but have higher FWHMs, and are blueshifted with respect to FLILs. The magnitude of the blueshift is correlated with the FWHM. This is another difference between the CLiF AGN and typical type 1 AGN.

The correlation of [O III] λ4363 and [Fe VII] λ6087 fluxes suggests that using the [O III] 4363/5007 emission-line flux ratio is not a reliable way to estimate temperature, at least for the CLiF AGN. Whether this is a problem for typical AGN requires the determination of the level of contamination of [O III] λ4363 from the CLiF region.

5.4 Emission region diagnostics

In order to investigate the physical conditions of both the FLIL and FHIL emission clouds, we used the photoionization code CLOUDY[9] (Ferland 1998) to create plane-parallel, single-slab photoionization models for the CLiF AGN emission lines. We assumed that the clouds were radiation bounded and had a solar composition.

[9] The version of CLOUDY used in this paper is c13.03.

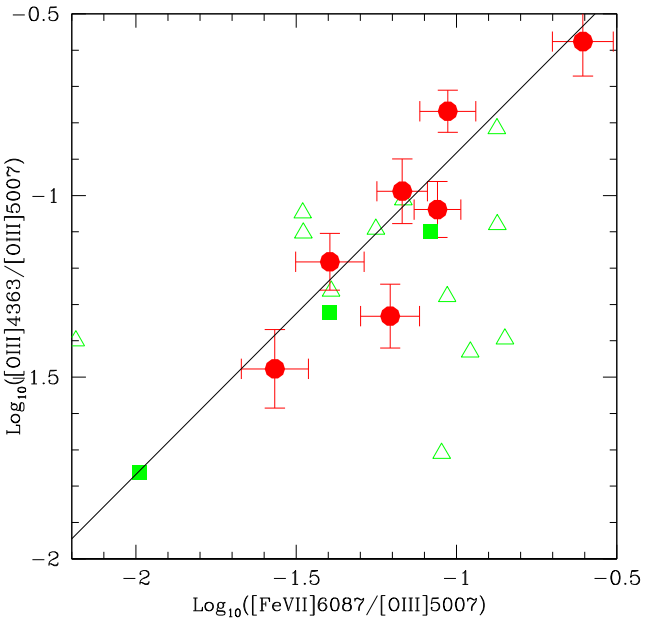

Figure 10. The strength of [O III] λ4363 versus [Fe VII] λ6087, normalized to [O III] λ5007. The CLiF AGN are indicated by red circles, the narrow-line Erkens, Appenzeller & Wagner (1997) objects by green squares, and the broad-line Erkens et al. (1997) objects by open green triangles. The solid line represents the best-fitting slope to the CLiF AGN.

We varied the ionization parameter (U) over the range $-2.5 \leq \log_{10}[U] \leq 0$, in increments of $\log_{10}[U] = 0.5$, and the hydrogen density ($n_{\rm H}$) over the range $3.0 \leq \log_{10}[n_{\rm H}\ {\rm cm}^{-3}] \leq 7.0$ in steps of $\log[n_{\rm H}\ {\rm cm}^{-3}] = 0.5$. The models were run assuming ionizing continuum power-law indices α −1.5, −1.2 and −0.8.[10] We used the 'table power law' command of CLOUDY to describe the input ionizing continuum spectral energy distribution (SED). This has a default spectral range from 10μm to 50 keV (Ferland 1998). The results are shown in Fig. 11. We do not show grids which assumes a power law of α=−1.5 or −0.8 because these models failed to reproduce the observed emission line ratios for the CLiF AGN.

We did not include dust grains when modelling the FHIL and FLIL clouds. This assumption is supported by the work of Ferguson, Korista & Ferland (1997), Nagao et al. (2003) and Nagao, Maiolino & Marconi (2006), who demonstrated that for a large sample of AGNs the observed FHIL strengths could not be reproduced in CLOUDY models that contain dust grains.

5.4.1 *FHILs*

First, we consider the FHILs. In Fig. 11(a), we plot a grid of [Fe VI] λ5176/[Fe VII] λ6086 versus [Fe VII]6086/5159 contours (iso-$n_{\rm H}$ and iso-U). We chose the [Fe VI] λ5176/[Fe VII] λ6086 ratio because it is sensitive to both U and the ionizing power-law, and we chose [Fe VII]6086/5159 because this is the only FHIL ratio whose emission lines were detected in all CLiF AGN, that is sensitive to density yet not as sensitive to variations in U. Note that [Fe VI] λ5176 was not detected in III Zw 77 and therefore it is not included on Fig. 11(a).

In Fig. 11(b), we plot a grid of [Fe VII]3760/6086 versus [Fe VII]6086/5159 contours. We chose [Fe VII]3760/6086 because it is sensitive to U.

[10] The emission is described by $F_\nu \propto \nu^{+\alpha}$, where α is the power-law spectral index.

All the ratios studied in Figs 11(a) and (b) consist of Fe lines. Therefore, they are completely free from the uncertainty in both the relative elemental abundance ratio, and the dust depletion factor.

Comparing the line ratios for the CLiF AGN with the grid models in Figs 11(a) and (b), we find the ratios are consistent with $n_{\rm H}$ in the range $4.5 < \log_{10}(n_{\rm H}\ {\rm cm}^{-3}) < 6.5$ and U in the range $-2.0 < \log[U] < 0$.

We cannot fit a U value for the FHIL emitting clouds of III Zw 77 (blue square). This is true for all assumed power laws for the ionizing continuum.

5.4.2 *Hα emitting region*

The observed Hα/Hβ ratio is very large (3.95–6.36 with the Case B value of 2.9) for a given Hγ/Hβ ratio in CLiF AGN. A plausible explanation is that the high density of the CLiF region in these objects, coupled with an extended partially ionized zone (Gaskell & Ferland 1984; Rose et al. 2011), will lead to significant collisional excitation of Hα in the partially ionized zones of clouds in the CLiF region. The other Balmer series emission lines, will not be enhanced as they have lower cross-sections for collisional excitation, as well as higher excitation temperatures (Gaskell & Ferland 1984; Osterbrock & Ferland 2006; Rose et al. 2011).

The conditions needed to produce the high observed Hα/Hβ flux ratios were investigated using CLOUDY. In Fig. 12, we plot a grid of Hα/Hβ versus [Fe X] λ6375/[Fe VII] λ6087 contours (iso-$n_{\rm H}$ and iso-U). We chose [Fe X] λ6375/[Fe VII] λ6087 because this ratio is sensitive to both U and the ionizing power-law, and because both [Fe VII] λ6087 and [Fe X] λ6375 have relatively high $n_{\rm crit}$ ($10^{7.6}$ and $10^{9.7}$ cm^{-3}, respectively), and are therefore not so sensitive to variations in the density.

Comparing the line ratios with the grid model, we find that the Hα/Hβ is consistent with densities in the range $6.0 < \log_{10}(n_{\rm H}\ {\rm cm}^{-3}) < 7.5$. These densities are higher than found in typical NLR ($\log(n_{\rm H}\ {\rm cm}^{-3}) < 4.0$; Osterbrock & Ferland 2006), and 0.5–1 dex higher than the FHIL clouds.

A high Hα/Hβ ratios could also be produced by lower metal abundances and/or a harder ionizing continuum (Gaskell & Ferland 1984; Rose et al. 2011). However, extremely low metallicities ($Z < 10^{-15}\ Z_\odot$) are required in order to reproduce these ratios. At these metallicities it is questionable whether strong Fe emission lines would be observed. In addition, altering the slope of the ionizing continuum results in the models being unable to reproduce the observed flux ratios of the FHILs.

The [Fe X] λ6375/[Fe VII] λ6087 ratios imply U in the range $-1.0 < \log[U] < -0.5$. This falls in to the range in U found for the FHILs in Section 5.4.1.

The ranges for U and $n_{\rm H}$ for the FHIL and Hα emitting clouds of each CLiF AGN are given in Table 5.

5.4.3 *FLILs*

Next, we consider the FLILs, i.e. the normal NLR lines. In Fig. 11(c), we plot a grid of [O I] λ6300/[S II] λ6317 versus [S II]6716/6731 contours. We chose [O I] λ6300/[S II] λ6317 because this ratio is sensitive to both the ionizing power-law and U, and we chose [S II]6716/6731 because it is sensitive to $n_{\rm e}$ (Osterbrock & Ferland 2006).

In Fig. 11(d), we plot a grid of [N II] λ6583/Hβ versus [S II]6716/6731 contours. We chose [N II] λ6583/Hβ because this ratio is sensitive to both the ionizing power-law and U. The [N II]

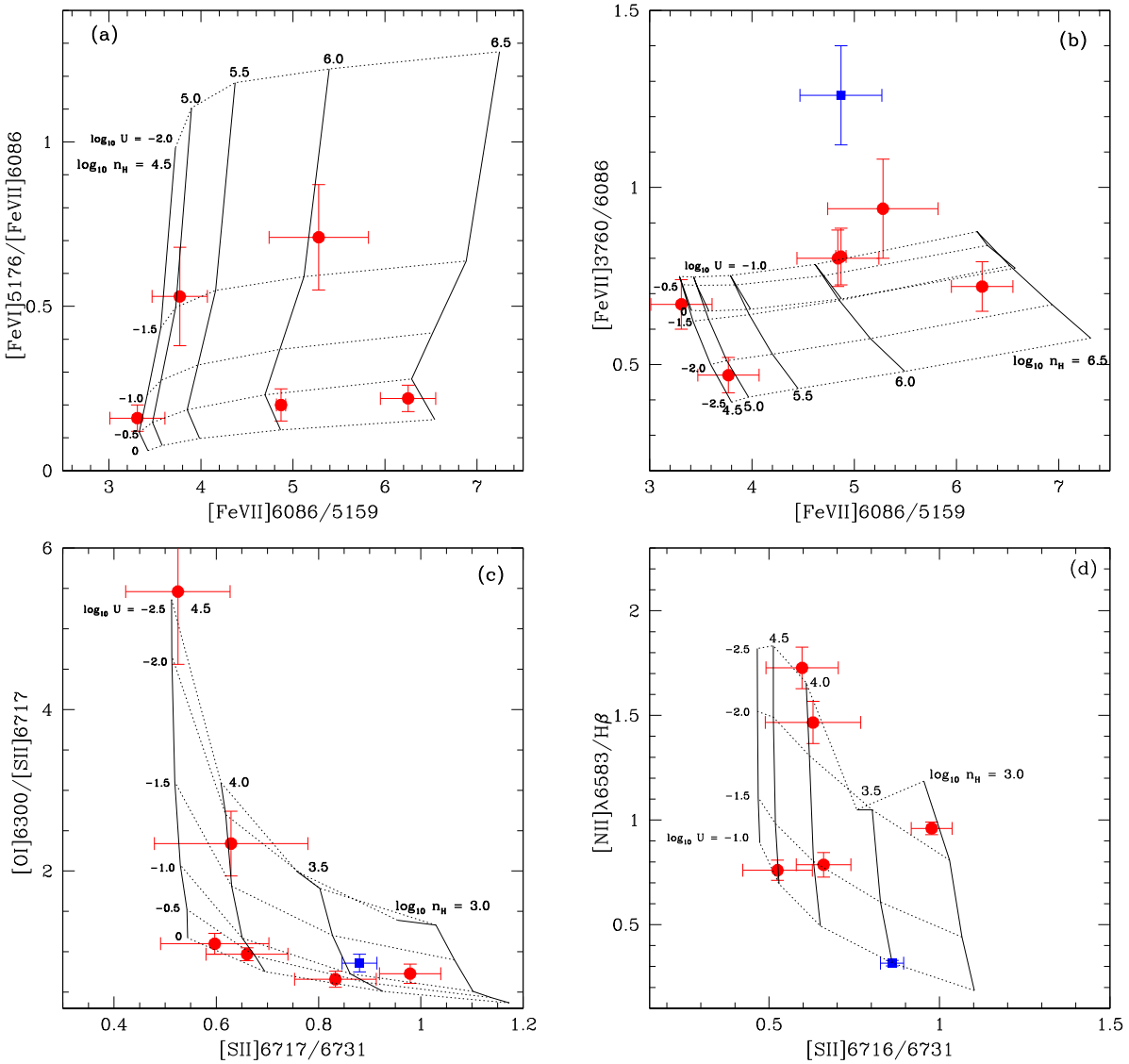

Figure 11. (a) Diagnostic plot for the FLIL region showing the measured [Fe VI] λ5176/[Fe VII] λ6087 versus [Fe VII]6087/5159 ratios for the CLiF AGN (red circles). III Zw 77 is indicated separately with a blue square. Isodensity lines are solid and isoionization parameter lines are dotted. (b) Diagnostic plot for the FLIL region showing the measured [Fe VII]3760/6087 versus [Fe VII]6087/5159 ratios. (c) Diagnostic plot for the FLIL region showing the measured [O I] λ6300/[S II] λ6717 versus [S II]6717/6731 ratios. (d) Diagnostic plot for the FLIL region showing the measured [N II] λ6583/Hβ versus [S II]6717/6731 ratios.

λ6583 emission is sensitive to the metallicity (Storchi-Bergmann 1991; Storchi-Bergmann et al. 1998). Decreasing the metallicity will increase the required U needed to reproduce the [N II] λ6583/Hβ ratio. However, this is a prominent FLIL ratio detected in all the CLiF AGN spectra.

The ratios for the CLiF AGN (red circles) are consistent for $n_{\rm H}$ in the range $3.0 < \log_{10}$ ($n_{\rm H}$ cm^{-3}) < 4.5 and U $-2.5 < \log\,[U] < 0$. The ranges for U and $n_{\rm H}$ for the FLIL region of each CLiF AGN are given in Table 6. These densities are consistent with those found for the NLRs of typical AGNs (e.g. Osterbrock & Ferland 2006). The lower end of the U range is consistent with those found for the NLR of AGN ($-2.5 < \log\,[U] < -2.0$; Bennert 2005). The FHIL densities exceed those found for the FLILs by 2 dex. While there is some overlap for the U required by the FLIL and FHIL ratios, overall the U required by the FHILs is higher by 0.5 dex assuming a solar metallicity.

5.4.4 *Comparisons of FHIL and FLIL region conditions*

Overall, the range of both U and $n_{\rm H}$ increase from the FLIL emitting region ($-2.5 < \log\,[U] < 0$, $3.0 < \log_{10}$ ($n_{\rm H}$ cm^{-3}) < 4.5) to the FHIL ($-2.0 < \log\,[U] < 0$, $4.5 < \log_{10}$ ($n_{\rm H}$ cm^{-3}) < 6.5) and boosted Hα emitting clouds ($-1.0 < \log\,[U] < -0.5$, $6.0 < \log_{10}$ ($n_{\rm H}$ cm^{-3}) < 7.5) for all the CLiF AGN. The median increase in U from the FLIL to the FHIL and boosted Hα emitting clouds is ~ 0.5 dex for the lower end of the U range, and $\sim$ 1.0 dex for the upper end. The median increase for $n_{\rm H}$ is $\sim$2 dex at lower end of the $n_{\rm H}$ range, and 3 dex for the upper end (see Tables 5 and 6).

In Fig. 13, we map the results of Section 5.4.1–5.4.3 on to $\log_{10}$ U versus $\log_{10}$ $n_{\rm H}$ space. The lines connect the FLIL (black circles), FHIL (red asterisks) and Hα (green squares) values for individual objects. We use the median U and $n_{\rm H}$ values to mark the positions of the CLiF AGN emission regions on Fig. 13, the error bars give the full ranges for these values. III Zw 77 and Tololo 0109-383

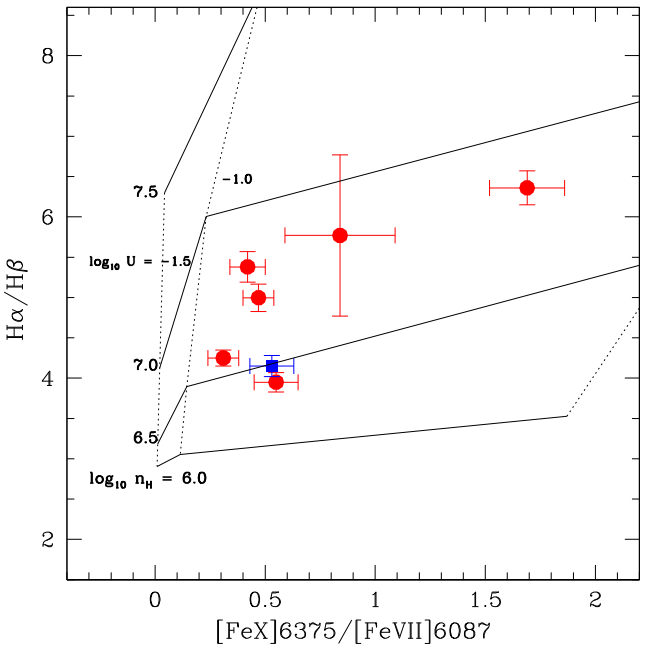

Figure 12. Diagnostic plot for the CLiF region showing the measured Hα/Hβ versus [Fe X] λ6375/[Fe VII] λ6087 ratios for the CLiF AGN (red circles). III Zw 77 is indicated separately with a blue square. Isodensity lines are solid and isoionization parameter lines are dotted.

have the same median U and $n_{\rm H}$ values for the FLIL emitting region and therefore overlap. Also ESO 138 G1, J1241+44 and J1641+43 have the same median U and $n_{\rm H}$ values for the FHIL emitting clouds. Finally, Q1131+16 and Tololo 0109-383 have the same median U and $n_{\rm H}$ values for the boosted Hα emitting clouds. Both the median U and $n_{\rm H}$ values increase from the FLIL emitting region to the FHIL emitting clouds and then to the Hα emitting clouds for all the CLiF AGN. However, we note that the range in U for the FHIL and boosted Hα emitting clouds overlap in all but two CLiF AGN: Mrk 1388 and J1241+44.

For comparison, we use the $n_{\rm H}$ and U measurements from Bennert (2005) for the NLR of normal AGN from spatially resolved VLT/FORS1 and NTT/EMMI spectroscopy for seven objects (5/7 type 1 AGN, open blue circles; 2/7 type 2 AGN, open green triangles). This work shows that the range of $n_{\rm H}$ ($2.5 < \log_{10} n_{\rm H} < 4.1$) measured for these NLRs are consistent with the range found for the FLILs of 5/7 of the CLiF AGN, as well as the typical density of the NLR ($2.5 < \log_{10} n_{\rm H} < 4.0$; Osterbrock & Ferland 2006). However, the U values for the Bennert (2005) measurements are consistent with only the low values found for the CLiF AGN ($-2.6 < \log_{10} U < -2.0$). The difference could be due to aperture effects, where

Table 6. $\log_{10} U$ and $\log_{10} n_{\rm H}$ ranges for the FLIL regions of the CLiF AGN. Both lower and upper subscripts indicate the lower and upper limits of the ranges, respectively.

Name	$U_{\rm lower}$	$U_{\rm upper}$	$n_{\rm H,\,lower}$	$n_{\rm H,\,upper}$
Q1131+16	−2.0	0	3.5	4.5
III Zw 77	−1.5	−1.0	3.0	4.0
Mrk 1388	−2.5	−1.5	3.5	4.5
ESO 138 G1	−2.5	−1.0	3.0	3.5
Tololo 0109-383	−1.5	−1.0	3.0	4.0
J1241+44	−2.5	−1.0	4.0	4.5
J1641+43	−2.5	0	3.5	4.5

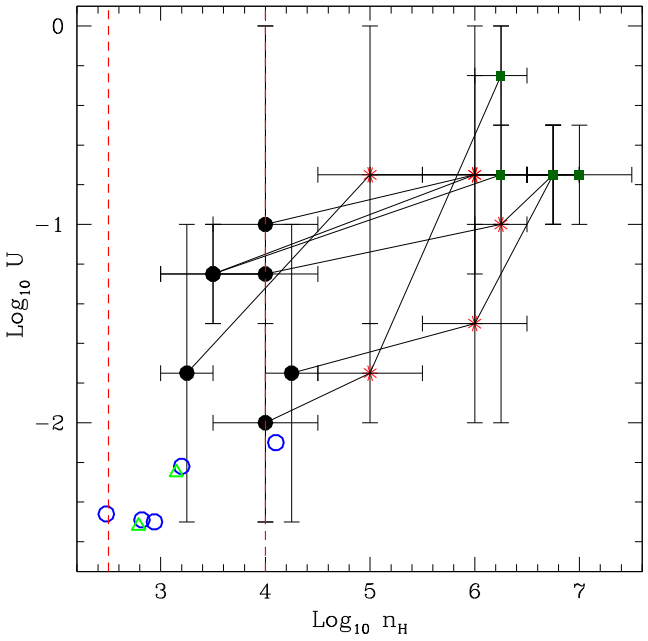

Figure 13. A comparison of the CLOUDY model results for the FLIL, FHIL and Hα emitting clouds for the CLiF AGN. We plot $\log_{10} U$ versus $\log_{10} n_{\rm H}$. The results for the FLILs are indicated by black circles, the results for the FHILs are indicated by red asterisks and the results for the Hα emitting clouds are indicated by green squares. The error bars present the U and $n_{\rm H}$ ranges. The results for individual objects are connected by solid lines. The results from the NLRs of the Bennert (2005) sample are indicated by open blue circles for the type 1 AGN, and open green triangles for the type 2 AGN. The expected range in density for the NLR is indicated by the red dotted lines (Osterbrock & Ferland 2006).

Table 5. $\log_{10} U$ and $\log_{10} n_{\rm H}$ ranges for the FHIL and Hα emitting clouds of the CLiF AGN. Both lower and upper subscripts indicate the lower and upper limits of the ranges, respectively.

	FHIL				Hα			
Name	$U_{\rm lower}$	$U_{\rm upper}$	$n_{\rm H,\,lower}$	$n_{\rm H,\,upper}$	$U_{\rm lower}$	$U_{\rm upper}$	$n_{\rm H,\,lower}$	$n_{\rm H,\,upper}$
Q1131+16	−1.5	0	5.5	6.5	−1.0	−0.5	6.5	7.0
III Zw 77	–	–	–	–	−1.0	−0.5	6.0	6.5
Mrk 1388	−2.0	−1.5	4.5	5.5	−1.0	−0.5	6.0	6.5
ESO 138 G1	−1.5	0	4.5	5.5	−1.0	−0.5	6.5	7.0
Tololo 0109-383	−1.5	0	5.5	6.5	−1.0	−0.5	6.5	7.5
J1241+44	−2.0	−1.0	5.5	6.5	−1.0	−0.5	6.5	7.0
J1641+43	−2.0	0	6.0	6.5	−1.0	−0.5	6.5	7.0

Table 7. Radial distance ($R_{\rm CLiF}$) and sublimation distance ($R_{\rm SUB}$) ranges for the CLiF AGN.

Name	$R_{\rm CLiF}$ lower	$R_{\rm CLiF}$ upper	$R_{\rm sub}$ 1800 K	$R_{\rm sub}$ 1500 K	$R_{\rm sub}$ 1200 K
Q1131+16	0.52 ± 0.01	16.49 ± 0.38	0.85 ± 0.05	1.51 ± 0.09	4.34 ± 0.25
III Zw 77	0.41 ± 0.01	2.33 ± 0.06	0.68 ± 0.04	1.09 ± 0.06	1.94 ± 0.11
Mrk 1388	0.33 ± 0.01	32.52 ± 0.74	0.16 ± 0.01	0.53 ± 0.03	1.52 ± 0.09
Tololo 0109-383	0.04 ± 0.01	2.03 ± 0.18	0.19 ± 0.01	0.53 ± 0.02	2.38 ± 0.14
J1241+44	0.09 ± 0.01	1.98 ± 0.13	0.10 ± 0.01	0.16 ± 0.02	0.29 ± 0.02
J1641+43	0.51 ± 0.02	28.65 ± 1.29	1.48 ± 0.09	2.43 ± 0.14	4.24 ± 0.24

we are sampling emission regions which are closer to the SMBH in the CLiF AGN using the SDSS spectroscopy, when compared with the spatially resolved spectroscopy of Bennert (2005).

5.5 The CLiF region radial distance

Given the computed U and $n_{\rm H}$ for the FHIL and boosted Hα emitting clouds CLiF AGN from Section 5.4, we can calculate a range of distances ($R_{\rm CLiF}$) to the CLiF regions given the ionizing luminosity ($L_{\rm ION}$):

$$R_{\rm CLiF} = \left(\frac{L_{\rm ION}}{4\pi U n_{\rm H} c \, \langle h\nu \rangle} \right)^{1/2}, \quad (1)$$

where U is the ionization parameter, $n_{\rm H}$ is the hydrogen density, $\langle h\nu \rangle$ is the mean ionizing photon energy,[11] and c is the speed of light. Note that we assume the CLiF emitting region includes both the boosted Hα emitting clouds and the strong FHIL emitting clouds, as both these unusual emission phenomena are seen for all CLiF AGN.

$L_{\rm ION}$ is estimated from $L_{[\rm O\,III]}$ using both the bolometric correction of Heckman et al. (2004) ($L_{\rm BOL} = 3500\, L_{[\rm O\,III]}$, with a variance of 0.38 dex), and the Elvis et al. (1994) SED ($L_{\rm BOL} \approx 3.1 \pm 0.2\, L_{\rm ION}$). Given that $L_{\rm ION}$ is proportional to $L_{[\rm O\,III]}$, and that we could not confidently correct $L_{[\rm O\,III]}$ for dust extinction, the computed radial distances to the CLiF emitting region must be considered lower limits.

Using this method, we find a range of radial distances for the CLiF emitting region: $0.04 < R_{\rm CLiF} < 32.5$ pc (Table 7). The uncertainties given were computed using the uncertainties for the [O III] λ5007 flux because they were the dominant source of uncertainty in the calculation. We could not calculate distance range for ESO 138 G1, because the spectrum in Alloin et al. (1992) was not flux calibrated. In addition, the distance range calculations for III Zw 77 relies solely on the CLOUDY grid presented in Fig. 12.

The lower end of this distance range is consistent with the inner torus MAGNUM reverberation results of Yoshii et al. (2014), who find AGN-torus distances of up to 0.1 pc. The higher end is consistent with disc radii measurements based on IR interferometry and high-resolution molecular line observations (e.g. Chou et al. 2007; Tristram et al. 2007), as well as results from fitting IR SEDs and spectroscopy (Alonso-Herrero et al. 2011).

We cannot make a direct comparison with the expected BLR radius for the CLiF AGN because we do not detect the BLR in the CLiF AGN spectra.

We also determine dust sublimation distances ($R_{\rm SUB}$) for the CLiF AGN using the relationship given by Elitzur (2008). We assume dust sublimation temperatures in the range $1200 < T_{\rm SUB} < 1800$ K,

[11] We assume a value of 56 eV for $\langle h\nu \rangle$, which is based on an ionizing power-law of -1.2, with the photon energy limits of 13.6 eV and 5 keV.

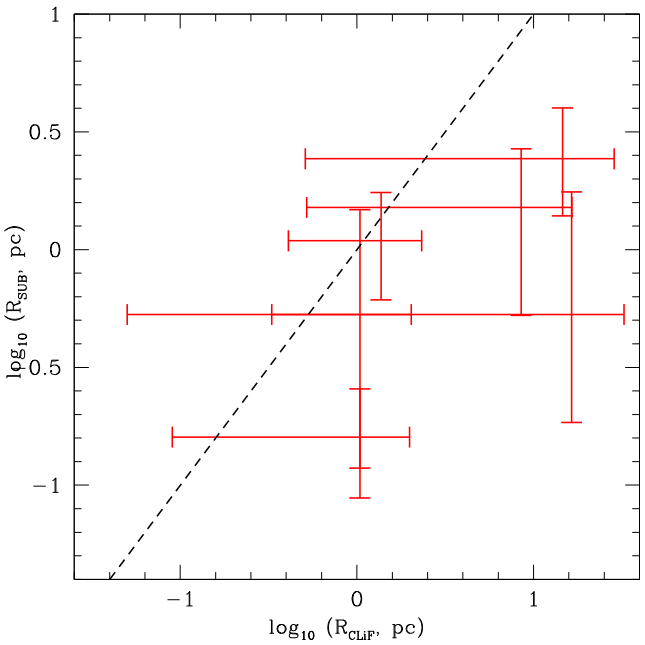

Figure 14. $\log_{10} R_{SUB}$ ranges versus $\log_{10} R_{\rm CLiF}$ ranges for the CLiF AGN (red lines). The dashed black line indicates a one-to-one ratio of $R_{\rm SUB}$ and $R_{\rm CLiF}$.

consistent with the expected range for torus dust grains (Barvainis 1987; Rodríguez-Ardila & Mazzalay 2006). The uncertainties were computed using both the uncertainty on the bolometric corrections and the uncertainties for the [O III] λ5007 flux.

Fig. 14 plots the $\log_{10} R_{\rm SUB}$ ranges versus the $\log_{10} R_{\rm CLiF}$ ranges (pc) for the CLiF AGN (red lines) given in Table 7. The x-axis error bars represent the $R_{\rm CLiF}$ distance ranges. These ranges intersect with the $R_{\rm SUB}$ ranges at the median $R_{\rm CLiF}$ value. The y-axis error bars represent the $R_{\rm SUB}$ distance ranges. The lowest $R_{\rm SUB}$ values are for $R_{\rm SUB}$ at a sublimation temperature of 1800 K, and the highest values are at a temperature of 1200 K. The $R_{\rm SUB}$ ranges intersect with the $R_{\rm CLiF}$ ranges at distances which assume a sublimation temperature of 1500 K. The dashed black line indicates the one-to-one relationship between $R_{\rm CLiF}$ and $R_{\rm SUB}$. Note that all $R_{\rm CLiF}$ ranges intersect with the one-to-one line.

However there is a caveat, $L_{[\rm O\,III]}$ has not been corrected for aperture effects. Due to the limited coverage of the SDSS fibre diameter (3 arcsec), a fraction of the total [O III] flux will be lost. Therefore, $L_{[\rm O\,III]}$ could be stronger than observed, which will subsequently increase both $L_{\rm ION}$ and $L_{\rm BOL}$, and therefore increase both $R_{\rm CLiF}$ and $R_{\rm SUB}$. But the increase in $R_{\rm CLiF}$ and $R_{\rm SUB}$ will be the same, and therefore the comparison of both parameters remain valid.

We find good agreement between the ranges for $R_{\rm CLiF}$ and $R_{\rm SUB}$ as both ranges overlap for the CLiF AGN. In addition the $R_{\rm CLiF}$ ranges

encompass the one-to-one ratios of R_{SUB} and R_{CLiF}. Although we use $L_{[O\,III]}$ to calculate both R_{CLiF} and R_{SUB}, the ratios between these two parameters do not have to agree.

6 DISCUSSION

6.1 The CLiF region – the inner wall of the torus?

Given that both the dust grain sublimation and CLiF emitting region distance ranges are consistent (Section 5.5), it is likely that the CLiF emitting region is closely associated with the inner wall of the torus, as suggested by Murayama & Taniguchi (1998) and Rose et al. (2011).

This CLiF location is supported by the observation that FHIL emission is rich in iron lines particularly [Fe VII], which can be enhanced relative to the dusty NLR (Mor, Netzer & Elitzur 2009) by the evaporation of dust grains in the inner torus wall, releasing the iron locked up in the grains (Pier & Voit 1995).

Rose et al. (2011) suggested that Q1131+16 is observed with our line of sight at a relatively large angle to the torus axis, so we have a maximal view of the far wall of the torus, while the AGN continuum is still obscured by the near side of the torus.

We emphasize that such a geometry is consistent with the relatively narrow FWHM and small velocity shifts of the FHILs, since the range of circular velocities associated with the torus will be restricted largely to transverse motions in the sky plane, and any vertical gas motions would be directed close to perpendicular to the line of sight (Rose et al. 2011).

6.2 Collisional excitation of Hα

In Section 5.1, we showed that the CLiF AGN occupy their own region on the BPT diagram due to a factor of ∼1.4–2.2 boosted Hα emission.

This boosting may be due to collisional excitation in the high-density CLiF region coupled with an extended partially ionized zone, so that hydrogen-like ions can be ionized (Gaskell & Ferland 1984; Rose et al. 2011). The other Balmer series emission lines, are not enhanced as they have lower cross-sections for collisional excitation, as well as higher excitation temperatures (Gaskell & Ferland 1984; Osterbrock & Ferland 2006; Rose et al. 2011). To explain the high Hα/Hβ ratio measured in the spectra of the CLiF AGN, requires a major (>35 per cent) contribution to the line flux of Hα from the CLiF region. Indeed, in Fig. 12 we investigated this possibility using CLOUDY modelling and found a required density range of $6.0 < \log_{10}\,(n_H\ cm^{-3}) < 7.5$, which is higher than expected for the NLR ($< 10^{4.5}$ cm^{-3}) and the FHIL emitting clouds ($10^{4.5} < n_H < 10^{6.5}$ cm^{-3}).

As there is a difference between the densities of the boosted Hα and FHIL emitting clouds, but no major difference in U (Section 5.4.4), we suggest that both sets of emission clouds are located in the CLiF region (possibly the inner torus wall, see Section 6.1), but there is a range of densities in the CLiF region, where the highest density clouds produce the boosted Hα flux.

In Fig. 6, we defined a box (red dotted line) to indicate the 'CLiF AGN Region' of the BPT diagram (limits: $-1.0 < \log_{10}([N\,II]/H\alpha) < -0.4$, and $0.65 < \log_{10}([O\,III]/H\beta) < 1.1$). Within these limits, the BOSS catalogue (Ahn et al. 2012) has 1284 CLiF AGN candidates. This population is just 0.5 per cent of the 259 008 objects in the AGN region of the BPT diagram (limits: $-0.4 < \log_{10}([N\,II]/H\alpha) < 1$, and $-0.1 < \log_{10}([O\,III]/H\beta) < 1.5$).

This region is based solely on the CLiF AGN studied in this paper. It is possible that higher levels of collisional excitation of Hα could push $\log_{10}([N\,II]/H\alpha)$ values lower than −1.0. These CLiF AGN candidates will be investigated in a further paper.

7 CONCLUSION

When compared to 'typical' AGN, the optical spectra of CLiF AGN show unusual properties in the sense that they are rich in emission lines, and have a remarkable variety of species.

Our analysis of seven CLiF AGN has shown that:

(1) The Hα Balmer emission line is boosted by a factor of ∼1.4–2.2 when compared to higher energy Balmer transitions, putting them in a distinct location on the BPT diagram.

(2) There is no difference between the velocity widths of the FLILs and FHILs.

(3) There is no evidence that the FHILs are blueshifted with respect to the FLILs.

(4) The [O III] λ4363 emission line is emitted from the same region as the FHILs in CLiF AGN as its emission flux is correlated with that of [Fe VII] λ6087.

(5) The FHILs of CLiF AGN are emitted from dense clouds ($10^{4.5} < n_H < 10^{6.5}$ cm^{-3}) when compared to the NLR.

(6) The boosted Hα emission lines of CLiF AGN are emitted from denser clouds ($10^{6.0} < n_H < 10^{7.5}$ cm^{-3}) when compared to the FHIL emitting clouds.

(7) We calculate small radial distances ($0.04 < R_{CLiF} < 32.5$ pc) to the CLiF emitting region, which are comparable to the sublimation distance for dust grains ($0.10 < R_{SUB} < 4.3$ pc).

A plausible model is that these objects are being viewed with a specific geometry which gives a maximal view of the inner wall on the far side of the torus, not at such a large angle from the disc plane that the BLR and continuum are exposed. In this scenario, the inner torus wall is the FHIL and boosted Hα emitting region, which consists of gas with a range of densities that are needed to produce both strong FHILs and boosted Hα emission.

We plan to follow up the CLiF AGN by (a) obtaining both X-ray and UV observations for the CLiF AGN, (b) modelling both the strength of the emission lines and kinematics of the CLiF emitting region, (c) using the BPT cleft to find more (Rose et al., in preparation), and (d) modelling the geometry (Glidden et al., in preparation).

ACKNOWLEDGEMENTS

We gratefully acknowledge Eugene Avrett, Thaisa Storchi Bergmann and Hagai Netzer for their insightful discussions. This work was supported in part by NASA grant NNX13AE88G. We thank the referee for useful comments and suggestions which improved this work substantially. The authors acknowledge the data analysis facilities provided by the Starlink Project, which is run by CCLRC on behalf of PPARC. This publication makes use of data products from the Two Micron All Sky Survey, which is a joint project of the University of Massachusetts and the Infrared Processing and Analysis Center/California Institute of Technology, funded by the National Aeronautics and Space Administration and the National Science Foundation. This publication also makes use of data products from NEOWISE, which is a project of the Jet Propulsion Laboratory/California Institute of Technology, funded by the Planetary Science Division of the National Aeronautics and Space Administration. This research has made use of the NASA/IPAC

Extragalactic Database (NED) which is operated by the Jet Propulsion Laboratory, California Institute of Technology, under contract with the National Aeronautics and Space Administration. Funding for SDSS-III has been provided by the Alfred P. Sloan Foundation, the Participating Institutions, the National Science Foundation, and the US Department of Energy Office of Science.

REFERENCES

Ahn C. P. et al., 2012, ApJS, 203, 21
Alloin D., Bica E., Bonatto C., Prugniel P., 1992, A&A, 226, 117
Alonso-Herrero A. et al., 2011, ApJ, 736, 82
Antonucci R. R. J., Miller J. S., 1985, ApJ, 297, 621
Appenzeller I., Wagner S. J., 1991, A&A, 250, 57
Baldwin J., Phillips M., Terlevich R., 1981, PASP, 93, 5
Barvainis R., 1987, ApJ, 320, 537
Bennert N., 2005, PhD thesis, Ruhr-Universität Bochum
Bolton A. S. et al., 2012, AJ, 144, 144
Calzetti D., Kinney A. L., Storchi-Bergmann T., 1994, ApJ, 429, 582
Chou R. C. Y. et al., 2007, ApJ, 670, 116
Civano F. et al., 2012, ApJ, 752, 49
De Robertis M. M., Osterbrock D. E., 1984, ApJ, 286, 171
Elitzur M., 2008, New Astron. Rev., 52, 274
Elvis M. et al., 1994, ApJS, 95, 1
Erkens U., Appenzeller I., Wagner S., 1997, A&A, 323, 707
Favata M., Hughes S. A., Holz D. E., 2004, ApJ, 607, 5
Ferguson J. W., Korista K. T., Ferland G. J., 1997, ApJS, 110, 287
Ferland G. J., 1998, PASP, 110, 761
Filippenko A. V., Halpern J. P., 1984, ApJ, 285, 458
Fosbury R. A., Sansom A. E., 1983, MNRAS, 204, 1231
Gaskell C. M., Ferland G. J., 1984, PASP, 96, 393
Gelbord J. M., Mullaney J. R., Ward M. J., 2009, MNRAS, 397, 172
Gezari S. et al., 2006, ApJ, 653, 25
Heckman T. M., Kauffmann G., Brinchmann J., Charlot S., Tremonti C., White S. D. M., 2004, ApJ, 613, 109
Kaler J. B., 1976, ApJS, 31, 517
Kauffmann G. et al., 2003, MNRAS, 346, 1055
Kewley L. J., Dopita M. A., Sutherland R. S., Heisler C. A., Trevena J., 2001, ApJ, 556, 121
Kewley L. J., Groves B., Kauffmann G., Heckman T., 2006, MNRAS, 372, 961
Komossa S. et al., 2009, ApJ, 701, 105
Krolik J. H., Kriss G. A., 1995, ApJ, 447, 512
Lauberts A., Valentijn E. A., 1989, The Surface Photometry Catalogue of the ESO-Uppsala Galaxies (ESOLV). ESO, Garching bei Munchen
Meinel A. B., Aveni A. F., Stockton M. W., 1975, Catalogue of Emission Lines in Astrophysical Objects. Optical Sciences Center. Univ. Arizona Press, Tucson
Mignoli M. et al., 2013, A&A, 556, 29
Mor R., Netzer H., Elitzur M., 2009, ApJ, 705, 298
Murayama T., Taniguchi Y., 1998, ApJ, 503, 115
Nagao T., Murayama T., Taniguchi Y., 2001, ApJ, 549, 155
Nagao T., Murayama T., Shioya Y., Taniguchi Y., 2003, AJ, 125, 1729
Nagao T., Maiolino R., Marconi A., 2006, A&A, 447, 863
Osterbrock D. E., 1981, ApJ, 249, 462
Osterbrock D. E., 1985, PASP, 97, 25O
Osterbrock D., Ferland G. J., 2006, Astrophysics of Gaseous Nebulae and Active Galactic Nuclei, 2nd edn. University Science Books, Mill Valley, CA
Penston M. V., Fosbury R. A. E., Boksenberg A., Ward M. J., Wilson A. S., 1984, MNRAS, 208, 347
Pier E. A., Voit G. M., 1995, ApJ, 450, 628
Reyes R. et al., 2008, AJ, 136, 237
Rodríguez-Ardila A., Mazzalay X., 2006, MNRAS, 367, 57
Rose M., Tadhunter C. N., Holt J., Ramos Almeida C., Littlefair S. P., 2011, MNRAS, 414, 3360
Smith N. et al., 2009, ApJ, 695, 1334
Storchi-Bergmann T., 1991, MNRAS, 249, 404
Storchi-Bergmann T., Schmitt H. R., Calzetti D., Kinney A. L., 1998, AJ, 115, 909
Tristram K. R. W., Meisenheimer K., Jaffe W., Cotton W. D., 2007, in Karas V., Matt G., eds, Proc. IAU Symp. 238, Black Holes from Stars to Galaxies – Across the Range of Masses. Cambridge Univ. Press, Cambridge, p. 93
Veilleux S., Osterbrock D. E., 1987, ApJS, 63, 295
Wang T., Zhou H., Komossa S., Wang H., Yuan W., Yang C., 2012, ApJ, 749, 115
Yoshii Y., Kobayashi Y., Minezaki T., Koshida S., Peterson B. A., 2014, ApJ, 784, 11

APPENDIX A: EMISSION LINE TABLES

Table A1. Line identifications for the SDSS spectrum of Mrk 1388. 'I_P presents the ionization potentials for the securely identified emission species. Flux ratios are relative to Hβ and are not corrected for reddening. Note that the fluxes presented here are from the double-Gaussian fitting model. Line IDs, Δv and FWHM are determined by fitting a single Gaussian to the emission lines. The total flux of the Hβ emission line is $(2.65 \pm 0.19) \times 10^{-15}$ erg s^{-1} cm^{-2} Å^{-1}. The column 'Gaussians' indicates the number of Gaussians required to fit the profile of the emission line.

Line ID	I_P (eV)	λ (Å)	λ_{SDSS} (Å)	F/F$_{H\beta}$	EW (Å)	Δv (km s^{-1})	FWHM (km s^{-1})	Gaussians
[Fe VII]	99.1	3758.9	3839.5 ± 0.1	0.16 ± 0.02	7.4	-42.8 ± 7.9	337.9 ± 20.1	2
H I	0	3770.6	3852.1 ± 0.5	0.03 ± 0.01	1.5	3.0 ± 43.0	154.2 ± 60.5	1
H I	0	3797.9	3878.9 ± 0.2	0.06 ± 0.01	3	-76.4 ± 17.0	380.4 ± 43.8	1
H I	0	3835.4	3918.4 ± 0.9	0.04 ± 0.01	2	10.7 ± 73.3	228.8 ± 111.6	1
[Ne III]	41.0	3868.8	3951.9 ± 0.0	1.30 ± 0.28	74.2	-33.0 ± 3.3	366.4 ± 8.1	2
[Fe V]	54.8	3891.3	3974.7 ± 0.3	0.28 ± 0.08	16	-47.8 ± 22.6	445.7 ± 54.9	2
[Ne III]	41.0	3967.5	4053.5 ± 0.0	0.44 ± 0.10	25.8	25.1 ± 2.7	379.0 ± 6.1	2
[S II]	10.4	4068.6	4155.8 ± 0.1	0.09 ± 0.02	3.9	-82.5 ± 10.2	382.4 ± 6.8	2
[S II]	10.4	4076.3	4163.3 ± 0.1	0.11 ± 0.03	4.8	-75.6 ± 12.5	382.4 ± 6.8	2
Hδ	13.6	4101.7	4189.3 ± 0.1	0.24 ± 0.05	10.5	-71.4 ± 25.1	382.0 ± 6.1	2

Table A1 – *continued*

Line ID	I_P (eV)	λ (Å)	λ_{SDSS} (Å)	$F/F_{H\beta}$	EW (Å)	Δv (km s^{-1})	FWHM (km s^{-1})	Gaussians
?		–	4310.5 ± 0.5	0.03 ± 0.01	1.6	–	194.2 ± 43.3	1
?		–	4322.0 ± 0.3	0.03 ± 0.01	1.6	–	206.3 ± 32.2	1
?		–	4335.5 ± 0.4	0.05 ± 0.01	2.6	–	376.7 ± 55.4	1
[O II]	13.6	4317.2	4411.5 ± 1.0	0.04 ± 0.01	2.1	70.2 ± 69.1	300.5 ± 103.0	1
Hγ	0	4340.5	4434.0 ± 0.1	0.49 ± 0.03	24.7	−20.6 ± 8.6	439.9 ± 26.7	2
[O III]	35.1	4363.2	4456.9 ± 0.1	0.56 ± 0.10	28.3	−38.5 ± 6.0	352.3 ± 15.7	2
HeI	0	4471.4	4569.4 ± 0.6	0.06 ± 0.02	2.9	92.9 ± 39.0	492.2 ± 79.8	1
?		–	4759.4 ± 0.5	0.04 ± 0.01	2	–	260.0 ± 50.6	1
He II	24.6	4685.7	4786.4 ± 0.1	0.34 ± 0.08	17	−30.2 ± 3.4	301.9 ± 8.1	2
Hβ	0	4861.3	4966.0 ± 0.1	–	30.8	−17.9 ± 3.8	350.8 ± 9.2	2
[O III]	35.1	4958.9	5065.9 ± 0.2	2.86 ± 0.19	88.2	−4.5 ± 10.3	341.5 ± 24.9	2
[O III]	35.1	5006.8	5114.9 ± 0.1	8.57 ± 0.21	264.5	–	357.0 ± 8.7	2
[Fe VII]	99.1	5159.0	5269.9 ± 0.3	0.09 ± 0.02	3	−32.0 ± 17.9	283.2 ± 31.3	2
[Fe VI]	75.0	5176.4	5288.2 ± 0.4	0.18 ± 0.05	6.1	−0.7 ± 22.0	94.4 ± 17.9	2
[N II]	14.5	5199.5	5311.5 ± 0.4	0.04 ± 0.01	1.5	17.3 ± 11.2	243.5 ± 38.3	1
[Fe VII]	99.1	5276.4	5390.0 ± 0.5	0.07 ± 0.02	3.5	−18.8 ± 27.6	269.4 ± 47.3	2
[Ca V]	67.3	5309.1	5422.8 ± 0.4	0.15 ± 0.04	7.5	−56.3 ± 24.4	539.6 ± 60.1	2
He II	24.6	–	5529.9 ± 0.5	0.06 ± 0.02	3	–	346.5 ± 56.5	1
[Fe VI]	75.0	5425.7	5540.9 ± 0.8	0.06 ± 0.02	3	−105.5 ± 44.0	464.6 ± 90.2	2
?		–	5557.9 ± 0.5	0.03 ± 0.01	1.6	–	250.3 ± 41.2	2
?		–	5578.2 ± 0.3	0.03 ± 0.01	1.6	–	109.4 ± 23.4	2
?		–	5739.7 ± 0.5	0.03 ± 0.01	1.6	–	213.2 ± 58.9	2
[Fe VI]	75.0	5677.0	5799.3 ± 0.7	0.04 ± 0.01	1.5	−14.3 ± 39.4	278.0 ± 82.0	1
[Fe VII]	99.1	5720.7	5844.1 ± 0.1	0.20 ± 0.03	6.2	−7.4 ± 4.2	285.2 ± 9.5	2
[N II]	14.5	5754.6	5878.8 ± 0.3	0.09 ± 0.02	3	−2.7 ± 17.8	423.0 ± 47.5	2
HeI	0	5875.6	6002.3 ± 0.1	0.12 ± 0.02	3.6	−12.8 ± 6.0	321.0 ± 14.7	2
?		–	6207.1 ± 1.5	0.05 ± 0.01	1.8	–	532.6 ± 159.1	1
[Fe VII]	99.1	6086.9	6217.7 ± 0.1	0.34 ± 0.05	11	−30.4 ± 4.5	284.2 ± 8.7	2
[O I]	0	6300.3	6436.6 ± 0.1	0.54 ± 0.09	14.8	9.4 ± 4.2	367.9 ± 11.5	2
[S III]	23.3	6312.1	6447.8 ± 0.4	0.10 ± 0.03	2.8	−30.6 ± 18.5	295.8 ± 36.8	2
[O I]	0	6363.8	6501.6 ± 0.3	0.15 ± 0.03	4.1	16.7 ± 14.2	293.1 ± 32.6	2
[Fe X]	233.6	6374.6	6511.1 ± 0.2	0.19 ± 0.03	5.2	−53.9 ± 10.3	263.2 ± 19.4	2
[N II]	14.5	6548.1	6691.8 ± 0.2	0.49 ± 0.08	15	100.1 ± 7.0	301.9 ± 4.9	2
Hα	0	6562.8	6704.2 ± 0.0	3.95 ± 0.12	121.1	−16.6 ± 0.7	288.4 ± 1.8	2
[N II]	14.5	6583.4	6726.4 ± 0.0	1.47 ± 0.16	45.1	33.6 ± 2.1	299.9 ± 4.9	2
?		–	6822.3 ± 0.7	0.04 ± 0.01	1.8	–	451.6 ± 61.0	1
[S II]	10.4	6716.4	6862.2 ± 0.1	0.23 ± 0.04	7.8	29.9 ± 3.8	327.9 ± 9.5	2
[S II]	10.4	6730.8	6876.6 ± 0.1	0.37 ± 0.09	11.2	19.4 ± 2.7	311.0 ± 6.3	2
?		–	7064.8 ± 1.1	0.12 ± 0.03	2	–	319.2 ± 86.6	1
?		–	7148.2 ± 3.0	0.13 ± 0.04	2	–	649.3 ± 182.9	1
[Ar V]	59.8	7005.9	7157.5 ± 0.5	0.13 ± 0.04	2	9.5 ± 23.5	251.9 ± 54.7	1
?		–	7197.5 ± 1.2	0.15 ± 0.03	2.1	–	624.5 ± 153.6	1
HeI	0	7065.7	7217.9 ± 0.3	0.07 ± 0.02	2	−18.6 ± 13.0	294.1 ± 31.7	1
[Ar III]	27.6	7135.8	7290.1 ± 0.1	0.12 ± 0.02	4	5.2 ± 4.2	355.0 ± 10.8	2
?		–	7309.4 ± 0.8	0.04 ± 0.01	1.5	–	428.4 ± 82.4	1
?		–	7326.5 ± 0.8	0.04 ± 0.01	1.5	–	348.5 ± 85.7	1
[O II]	13.6	7319.9	7478.8 ± 0.5	0.15 ± 0.03	5.1	31.2 ± 20.0	521.4 ± 48.0	2
[O II]	13.6	7330.2	7490.2 ± 0.5	0.18 ± 0.06	6.1	68.7 ± 20.1	340.3 ± 31.8	2
?		–	7537.2 ± 1.4	0.07 ± 0.02	2.5	–	454.1 ± 126.6	1
?		–	7773.2 ± 0.5	0.03 ± 0.01	1.4	–	196.4 ± 29.2	1
?		–	7919.9 ± 1.2	0.07 ± 0.01	2.3	–	677.1 ± 177.7	1
[Fe XI]	262.1	7891.8	8061.4 ± 0.2	0.13 ± 0.03	4.3	−31.9 ± 6.5	237.7 ± 12.5	2

Table A2. Line identifications for the SDSS spectrum of III Zw 77. 'I_P presents the ionization potentials for the securely identified emission species. Flux ratios are relative to Hβ and are not corrected for reddening. Note that the fluxes presented here are from the double-Gaussian fitting model. Line IDs, Δv and FWHM are determined by fitting a single Gaussian to the emission lines. The total flux of the Hβ emission line is $(2.52 \pm 0.09) \times 10^{-14}$ erg s^{-1} cm^{-2} Å^{-1}. The column 'Gaussians' indicates the number of Gaussians required to fit the profile of the emission line.

Line ID	I_P (eV)	λ (Å)	λ_{SDSS} (Å)	F/F$_{H\beta}$	EW (Å)	Δv	FWHM	Gaussians
[O II]	13.6	3727.4	3854.0 ± 0.1	0.63 ± 0.07	8.7	−28.2 ± 7.8	413.3 ± 15.4	2
[Fe VII]	99.1	3758.9	3887.3 ± 0.1	0.49 ± 0.05	6.8	17.4 ± 11.1	450.2 ± 27.5	2
[Fe V]	54.8	3839.3	3968.0 ± 0.8	0.07 ± 0.01	2.1	−164.1 ± 61.2	409.0 ± 109.1	1
[Ne III]	41.0	3868.8	4000.6 ± 0.0	1.33 ± 0.24	19.2	−11.9 ± 2.9	346.2 ± 6.9	2
[Fe V]	54.8	3891.3	4023.9 ± 0.2	0.41 ± 0.08	5.9	−5.6 ± 16.8	486.2 ± 33.1	2
[Ne III]	41.0	3967.5	4103.1 ± 0.2	0.16 ± 0.02	2.8	21.3 ± 12.2	183.7 ± 26.7	1
?		–	4109.1 ± 0.5	0.49 ± 0.12	8.6	–	1388.5 ± 77.0	2
[S II]	10.4	4068.6	4208.2 ± 0.3	0.12 ± 0.02	2.1	64.2 ± 21.7	464.2 ± 53.3	1
[S II]	10.4	4076.3	4216.2 ± 0.3	0.03 ± 0.01	0.8	63.9 ± 21.6	463.2 ± 53.5	1
Hδ	0	4101.7	4242.1 ± 0.1	0.25 ± 0.05	4.4	35.9 ± 8.5	381.2 ± 21.0	2
Hδ_B	0	4101.7	4233.0 ± 1.4	0.59 ± 0.03	10.4	−643.5 ± 100.1	2546.1 ± 171.9	2
[O II]	13.6	4317.2	4465.9 ± 0.5	0.15 ± 0.04	3.5	99.4 ± 32.6	345.2 ± 10.5	2
Hγ	0	4340.5	4489.0 ± 0.1	0.34 ± 0.04	7.8	34.7 ± 6.7	343.0 ± 10.4	2
Hγ_B	0	4340.5	4479.3 ± 0.8	0.70 ± 0.05	16.1	−648.3 ± 55.4	2328.9 ± 168.4	2
[O III]	35.1	4363.2	4512.2 ± 0.1	0.45 ± 0.05	10.4	13.9 ± 4.9	340.9 ± 10.3	2
HeI	0	4471.4	4625.7 ± 0.7	0.04 ± 0.01	1.9	119.3 ± 47.4	391.5 ± 79.7	1
?		–	4818.0 ± 0.5	0.06 ± 0.01	1.6	–	279.6 ± 70.3	1
He II	24.6	4685.7	4845.8 ± 0.1	0.44 ± 0.07	7.0	17.0 ± 8.2	469.4 ± 24.4	2
[Ar IV]	40.7	4712.6	4902.0 ± 1.2	0.03 ± 0.01	1.4	8.4 ± 75.9	113.5 ± 131.9	1
Hβ	0	4861.3	5027.9 ± 0.1	–	15.4	50.3 ± 3.8	386.3 ± 10.4	2
Hβ_B	0	4861.3	5016.6 ± 0.7	2.03 ± 0.09	31.3	−624.8 ± 41.3	2628.4 ± 87.8	2
[Fe VII]	99.1	4893.4	5061.5 ± 0.8	0.03 ± 0.01	1.3	70.9 ± 51.8	163.9 ± 69.6	1
[Fe IV]	30.7	4903.1	5070.0 ± 1.6	0.05 ± 0.01	2.7	−16.5 ± 100.4	651.9 ± 249.1	1
[O III]	35.1	4958.9	5128.0 ± 0.1	1.94 ± 0.19	29.9	1.3 ± 6.8	289.3 ± 4.8	2
[O III]	35.1	5006.8	5177.5 ± 0.0	5.82 ± 0.29	89.6	–	285.6 ± 4.7	2
[Fe VII]	99.1	5159.0	5334.9 ± 0.4	0.08 ± 0.01	3.2	−0.2 ± 20.9	226.2 ± 35.0	2
[Fe VII]	99.1	5276.4	5456.9 ± 0.7	0.06 ± 0.01	3.2	29.2 ± 40.0	308.4 ± 88.6	2
[Ca V]	67.3	5309.1	5489.0 ± 0.9	0.22 ± 0.05	8.9	−60.7 ± 52.7	975.0 ± 159.7	2
[Fe VII]	99.1	5720.7	5916.7 ± 0.1	0.23 ± 0.03	5.6	46.3 ± 7.5	340.9 ± 17.4	2
HeI	0	5875.6	6077.7 ± 1.2	0.24 ± 0.04	5.8	86.4 ± 60.3	697.3 ± 99.1	2
?		–	6281.8 ± 0.7	0.05 ± 0.01	2.9	–	348.5 ± 8.8	1
[Fe VII]	99.1	6086.6	6294.9 ± 0.1	0.39 ± 0.05	9.5	21.0 ± 3.9	347.6 ± 8.8	2
[O I]	0	6300.3	6515.1 ± 0.1	0.13 ± 0.01	3.0	−2.2 ± 6.0	236.8 ± 12.2	1
[S III]	23.3	6312.1	6527.0 ± 0.7	0.03 ± 0.01	1.0	−15.7 ± 34.6	187.6 ± 47.0	1
[O I]	0	6363.8	6581.1 ± 0.3	0.04 ± 0.01	1.1	13.6 ± 14.9	188.3 ± 22.0	1
[Fe X]	233.6	6374.6	6592.8 ± 0.2	0.21 ± 0.05	4.8	36.7 ± 7.1	415.8 ± 18.8	2
[N II]	14.5	6548.1	6806.8 ± 0.4	0.28 ± 0.07	5.3	−50.4 ± 18.0	373.2 ± 12.4	2
Hα	0	6562.8	6787.9 ± 0.1	4.15 ± 0.13	81.5	58.7 ± 3.4	374.4 ± 12.5	2
Hα_B	0	6562.8	6773.0 ± 1.0	7.09 ± 1.84	139.2	−658.5 ± 46.7	2517.4 ± 76.5	2
[N II]	14.5	6583.4	6770.3 ± 0.4	0.89 ± 0.21	15.9	−50.5 ± 18.1	375.6 ± 12.5	2
[S II]	10.4	6716.4	6945.7 ± 0.1	0.15 ± 0.03	3.0	11.7 ± 3.4	189.9 ± 6.5	2
[S II]	10.4	6730.8	6960.5 ± 0.1	0.17 ± 0.03	3.1	8.8 ± 3.3	207.4 ± 6.3	2
[Ar V]	59.8	7005.9	7243.0 ± 1.3	0.11 ± 0.02	2.8	−73.8 ± 55.3	1090.2 ± 159.2	1
?		–	7282.6 ± 1.2	0.12 ± 0.03	3.0	–	990.5 ± 135.5	1
HeI	0	7065.7	7307.8 ± 0.4	0.11 ± 0.02	2.8	49.5 ± 17.9	477.5 ± 47.8	1
[Ar III]	27.6	7135.8	7379.3 ± 0.2	0.08 ± 0.02	2.5	8.5 ± 7.7	170.6 ± 12.3	1
[O II]	13.6	7319.9	7569.1 ± 0.5	0.06 ± 0.01	2.4	−16.7 ± 22.0	298.9 ± 43.1	1
[O II]	13.6	7330.2	7581.1 ± 0.7	0.04 ± 0.01	1.8	36.7 ± 30.1	234.9 ± 83.7	1
?		–	7628.1 ± 1.4	0.03 ± 0.01	1.7	–	342.3 ± 80.1	1
[Fe XI]	262.1	7891.8	8161.5 ± 0.3	0.13 ± 0.04	7.4	21.7 ± 12.1	320.2 ± 28.9	2
?		–	8738.4 ± 1.0	0.05 ± 0.01	2.4	–	304.2 ± 76.9	1

Table A3. Line identifications for the SDSS spectrum of J1241+44. 'I_P presents the ionization potentials for the securely identified emission species. Flux ratios are relative to Hβ and are not corrected for reddening. Note that the fluxes presented here are from the double-Gaussian fitting model. Line IDs, Δv and FWHM are determined by fitting a single Gaussian to the emission lines. The total flux of the Hβ emission line is $(4.96 \pm 0.30) \times 10^{-16}$ erg s^{-1} cm^{-2} Å^{-1}. The column 'Gaussians' indicates the number of Gaussians required to fit the profile of the emission line.

Line ID	I_P (eV)	λ (Å)	λ_{SDSS} (Å)	F/F$_{H\beta}$	EW (Å)	Δv	FWHM	Gaussians
[O II]	13.6	3727.4	3885.9 ± 0.5	0.77 ± 0.18	7.7	104.2 ± 44.0	433.1 ± 92.7	2
[Fe VII]	99.1	3758.9	3917.7 ± 0.2	1.09 ± 0.15	13.9	17.2 ± 3.7	282.4 ± 40.2	2
[Ne III]	41.0	3868.8	4031.7 ± 0.1	1.57 ± 0.15	13.7	−27.8 ± 8.8	256.3 ± 22.2	2
Hγ	0	4340.5	4523.2 ± 0.3	0.47 ± 0.04	3.4	−31.8 ± 18.6	205.5 ± 34.8	2
[O III]	35.1	4363.2	4547.1 ± 0.2	1.3 ± 0.13	8.3	−17.2 ± 10.8	287.9 ± 29.6	2
He II	24.6	4685.7	4883.4 ± 0.1	0.87 ± 0.09	4.5	−3.1 ± 9.3	227.4 ± 18.4	2
[Ne III]	41.0	4815.9	5017.9 ± 0.3	0.13 ± 0.04	2.8	−73.3 ± 21.5	89.7 ± 38.8	2
Hβ	0	4861.3	5066.2 ± 0.1	–	5.1	−13.2 ± 5.3	178.5 ± 12.8	2
[O III]	35.1	4958.9	5168.2 ± 0.1	1.39 ± 0.11	7.5	2.4 ± 4.8	206.1 ± 11.7	2
[O III]	35.1	5006.8	5218.0 ± 0.0	4.34 ± 0.28	22.6	–	215.8 ± 4.7	2
[Fe VII]	99.1	5159.0	5375.0 ± 0.4	0.21 ± 0.07	2.1	−97.7 ± 22.4	141.3 ± 67.3	2
[Fe VI]	75.0	5176.4	5394.8 ± 0.3	0.79 ± 0.18	7.9	−3.8 ± 17.8	147.0 ± 38.9	2
[Ca V]	67.3	5309.1	5531.4 ± 1.1	0.27 ± 0.07	2.1	−94.0 ± 59.8	564.4 ± 136.9	2
?		–	5766.6 ± 0.3	0.29 ± 0.06	2.2	–	168.7 ± 36.4	2
?		–	5856.0 ± 0.4	0.27 ± 0.07	2.1	–	157.2 ± 47.3	2
[Fe VII]	99.1	5720.7	5963.0 ± 0.2	0.64 ± 0.09	4.1	44.6 ± 10.1	184.4 ± 27.7	2
HeI	0	5875.6	6124.2 ± 0.5	0.17 ± 0.04	1.9	30.6 ± 12.1	159.0 ± 16.5	2
[Fe VII]	99.1	6086.9	6343.6 ± 0.1	1.11 ± 0.08	5.2	−10.0 ± 4.5	209.2 ± 11.0	2
?		–	6443.5 ± 0.5	0.11 ± 0.04	1.6	–	139.1 ± 52.0	2
[O I]	0	6300.3	6566.0 ± 0.2	0.61 ± 0.06	3.2	−5.8 ± 7.3	186.9 ± 17.5	2
[O I]	0	6363.8	6632.4 ± 0.3	0.21 ± 0.04	1.3	0.9 ± 13.5	147.9 ± 2.4	2
[Fe X]	233.6	6374.6	6643.7 ± 0.1	1.88 ± 0.12	8.7	5.9 ± 2.5	219.9 ± 6.2	2
[Ar V]	59.8	6435.1	6707.0 ± 0.5	0.13 ± 0.04	1.5	16.0 ± 25.4	176.5 ± 50.3	2
[N II]	14.5	6548.1	6823.7 ± 0.7	0.17 ± 0.06	1.3	−29.9 ± 30.0	170.5 ± 51.2	2
Hα	0	6562.8	6839.7 ± 0.0	6.36 ± 0.21	30.5	−3.1 ± 1.1	213.7 ± 2.8	2
[N II]	14.5	6583.4	6861.2 ± 0.2	0.71 ± 0.08	3.9	−2.9 ± 7.8	180.7 ± 18.5	2
[S II]	10.4	6716.4	6999.0 ± 0.5	0.11 ± 0.03	1	−33.9 ± 20.1	78.1 ± 97.2	2
[S II]	10.4	6730.8	7014.8 ± 0.4	0.22 ± 0.04	2	−3.3 ± 17.8	181.8 ± 35.5	2
[Fe XI]	262.1	6985.2	7278.5 ± 0.3	0.24 ± 0.04	2.4	−61.5 ± 13.0	142.2 ± 25.1	2
[Ar V]	59.8	7005.9	7299.5 ± 0.8	0.24 ± 0.06	2.4	−82.8 ± 32.6	260.6 ± 65.5	2
[Ar III]	27.6	7135.8	7436.6 ± 0.4	0.21 ± 0.07	2	−13.3 ± 16.6	144.6 ± 74.0	2
[O II]	13.6	7319.9	7629.2 ± 0.5	0.32 ± 0.08	2.2	14.1 ± 20.3	195.1 ± 62.2	2
[O II]	13.6	7330.2	7639.7 ± 0.6	0.21 ± 0.06	1.9	6.8 ± 25.5	175.5 ± 50.5	2
[Fe XI]	262.1	7891.8	8225.0 ± 0.1	1.45 ± 0.13	7.6	4.3 ± 5.6	208.3 ± 15.6	2

Table A4. Line identifications for the SDSS spectrum of 1641+43. 'I_P presents the ionization potentials for the securely identified emission species. Flux ratios are relative to Hβ and are not corrected for reddening. Note that the fluxes presented here are from the double-Gaussian fitting model. Line IDs, Δv and FWHM are determined by fitting a single Gaussian to the emission lines. The total flux of the Hβ emission line is $(2.26 \pm 0.10) \times 10^{-15}$ erg s^{-1} cm^{-2} Å^{-1}. The column 'Gaussians' indicates the number of Gaussians required to fit the profile of the emission line.

Line ID	I_P (eV)	λ (Å)	λ_{SDSS} (Å)	F/F$_{H\beta}$	EW (Å)	Δv	FWHM	Gaussians
[Ne V]	97.1	3345.6	4084.2 ± 0.4	0.46 ± 0.18	16.0	−174.3 ± 133.5	744.5 ± 99.6	2
[Ne V]	97.1	3425.9	4182.1 ± 0.2	1.73 ± 0.13	47.9	−164.2 ± 62.5	858.8 ± 37.1	2
[O II]	13.6	3727.4	4552.4 ± 0.2	0.48 ± 0.02	20.6	−8.6 ± 0.2	490.3 ± 41.3	2
[Fe VII]	99.1	3758.9	4588.8 ± 0.8	0.36 ± 0.09	15.2	−149.5 ± 222.3	809.3 ± 129.1	2
[Ne III]	41.0	3868.8	4725.7 ± 0.6	0.95 ± 0.04	41.9	22.1 ± 1.3	827 ± 61.4	2
[Fe V]	54.8	3891.3	4752.2 ± 0.8	0.20 ± 0.08	8.3	−40.0 ± 3.8	741 ± 68.9	2
[Ne III]	41.0	3967.5	4846.0 ± 0.4	0.30 ± 0.04	12.9	6.9 ± 0.3	369.9 ± 58.2	2
?		–	4854.0 ± 0.8	0.07 ± 0.01	3.1	−102.3 ± 111.9	369.2 ± 58.1	1
Hδ	0	4101.7	5009.9 ± 1.0	0.18 ± 0.04	6.6	7.2 ± 0.7	665.7 ± 224.4	2
Hγ	0	4340.5	5303.6 ± 0.8	0.40 ± 0.03	15.8	122.0 ± 168.0	1222.0 ± 124.4	2
[O III]	35.1	4363.2	5329.0 ± 0.7	0.39 ± 0.04	15.6	−14.7 ± 2.2	819.2 ± 77.7	2
[O II]	13.6	4414.9	5396.9 ± 2.7	0.15 ± 0.04	5.9	251.5 ± 120.0	710.0 ± 59.2	2
He II	24.6	4685.7	5721.2 ± 0.7	0.30 ± 0.03	9.6	−102.3 ± 111.9	680.9 ± 73.6	2
Hβ	0	4861.3	5937.8 ± 0.3	–	35.0	8.3 ± 0.3	721.3 ± 39.8	2
[O III]	35.1	4958.9	6057.3 ± 0.4	1.77 ± 0.08	67.3	26.9 ± 4.3	626.3 ± 45.3	2
[O III]	35.1	5006.8	6115.4 ± 0.1	5.31 ± 0.25	201.9	–	692.3 ± 16.5	2
[Fe VII]	99.1	5159.0	6302.5 ± 0.2	0.08 ± 0.01	3.5	64.1 ± 10.9	546.0 ± 24.8	2

Table A4 – *continued*

Line ID	I_P (eV)	λ (Å)	λ_{SDSS} (Å)	$F/F_{H\beta}$	EW (Å)	Δv	FWHM	Gaussians
[Fe VI]	75.0	5176.4	6315.9 ± 1.1	0.11 ± 0.02	4.0	−312.7 ± 200.0	543.4 ± 104.7	2
[Fe VII]	99.1	5720.7	6985.9 ± 0.9	0.25 ± 0.04	10.2	−59.3 ± 63.6	788.0 ± 181.7	2
[Fe VII]	99.1	6086.9	7430.2 ± 1.0	0.50 ± 0.12	19.4	−174.5 ± 78.0	904.1 ± 92.9	2
[O I]	0	6300.3	7698.9 ± 2.4	0.21 ± 0.05	6.6	144.5 ± 50.0	648.2 ± 237.2	2
[O I]	0	6363.8	7778.2 ± 3.4	0.07 ± 0.02	1.7	210.5 ± 100.0	954.5 ± 316.7	1
[Fe X]	233.6	6374.6	7785.7 ± 0.7	0.21 ± 0.05	7.2	−39.9 ± 8.2	814 ± 85.2	2
[N II]	14.5	6548.1	7997.1 ± 0.5	0.57 ± 0.1	17.6	−29.0 ± 10.0	364.4 ± 69.9	2
Hα	0	6562.8	8017.7 ± 1.6	5.38 ± 0.19	166.0	60.8 ± 15.8	476.8 ± 38.2	2
[N II]	14.5	6583.4	8040.2 ± 0.5	1.71 ± 0.11	52.8	−29.4 ± 10.3	362.0 ± 69.4	2
[S II]	10.4	6716.4	8203.6 ± 1.0	0.19 ± 0.05	8.0	5.8 ± 0.7	479.7 ± 170.7	2
[S II]	10.4	6730.8	8221.3 ± 1.3	0.30 ± 0.04	5.0	10.6 ± 3.2	350.3 ± 84.5	2

APPENDIX B: UNKNOWN LINE TABLE

Table B1. Emission lines without a secure ID for the SDSS spectra. Information for Q1131+16 is presented to highlight any overlap.

λ_{rest} (Å)	Mrk 1388	III Zw 77	J1241+44	J1641+43	Q1131+16
3973.5		Y		Y	
4219.4	Y				
4230.6	Y				
4243.8	Y				
4659.1		Y			
5413.0	Y				Y
5440.4	Y				
5460.3	Y				
5533.1			Y		Y
5618.6	Y		Y		Y
6075.1	Y	Y			
6182.6			Y		
6678.1	Y				
6915.4	Y				
6997.1	Y				
7043.9	Y	Y			
7154.9	Y				Y
7171.6	Y				
7377.1	Y	Y			
7608.8	Y				
7752.4	Y				
8450.0		Y			

This paper has been typeset from a TEX/LATEX file prepared by the author.